Straddle-type heterostructure films endow titanium implant with NIR photocatalysis property for rapid sterilization

Shiwei Guan [a,b,1], Zhenhao Hou [a,b,1], Ji Tan [a,*], Xianming Zhang [a], Junyu Liu [a], Huihui Du [a,b], Hongqin Zhu [a,c], Yuqin Qiao [a], Zixiao Liu [a], Xuanyong Liu [a,b,d,**]

[a] State Key Laboratory of High Performance Ceramics and Superfine Microstructure, Shanghai Institute of Ceramics, Chinese Academy of Sciences, Shanghai 200050, China
[b] Center of Materials Science and Optoelectronics Engineering, University of Chinese Academy of Sciences, Beijing 100049, China
[c] Department of Materials Science, Fudan University, Shanghai 200433, China
[d] School of Chemistry and Materials Science, Hangzhou Institute for Advanced Study, University of Chinese Academy of Sciences, 1 Sub-lane Xiangshan, Hangzhou 310024, China

ABSTRACT

Near-infrared (NIR) light-triggered photocatalysis antibacterial therapy has attracted significant attention. Herein, we designed a straddle-type heterostructure film of ZnS/Ag$_2$S nanorod on the titanium implant, which showed excellent NIR photocatalytic ability. Under NIR, the electrons of Ag$_2$S cascaded jump to ZnS conduction band (CB), and the electron of ZnS was half-jumped to Ag$_2$S valence band (VB). The VB of Ag$_2$S acted as a consumption platform for the holes of Ag$_2$S and the electrons of ZnS, improving photocatalytic efficiency. To prove the feasibility of this mechanism, another straddle-type heterostructure of ZnS/Bi$_2$S$_3$ with similar energy band structure was fabricated, and its NIR photocatalytic ability was also distinctly enhanced. Furthermore, the ZnS/Ag$_2$S heterostructure films rapidly removed bacteria *in vitro* and *in vivo* under the NIR irradiation. This work innovatively discovered NIR photocatalytic effect of the straddle-type heterostructure, which complemented the design of heterostructures in photocatalysis.

1. Introduction

Bacterial infection in the course of surgery has developed as an essential killer of biomedical implant failure. The most commonly-used antibiotic therapy easily leads to the proliferation of drug-resistant bacteria [1,2]. Therefore, the antimicrobial-based film is an urgent requirement for the implant surface. Currently, photocatalysis antibacterial therapy, as a repaid and effective method, has attracted significant attention. When photosensitive materials are exposed to light, the escaped electrons or holes are captured by adjacent O_2 or OH^-, generating ROS ($\bullet O_2^-$, $\bullet OH$, and $^1O_2$) to poison the bacteria effectively [3,4]. However, most photocatalytic materials are excited by ultraviolet or visible light, and the low penetration depth limits ultraviolet and visible light application in deep location therapy [3]. Near-infrared (NIR) light has an excellent penetrating ability to overcome this shortcoming [4].

Thus, semiconductor materials with narrow bandgaps have become ideal for NIR-triggered photocatalytic therapy [5–7]. Unfortunately, these single-group photocatalysts are prone to momentarily recombining photogenerated electrons and holes, leading to minimal photocatalytic reaction.

Combining with other functional materials to form heterostructure is a reliable strategy for facilitating photoelectron-hole separation. The construction of heterostructure has been three fascinating photocatalysis strategies, including type-II, Z-scheme, and P-N heterojunctions [8,9]. The type-II heterostructure is a staggered band alignment, and the photogenerated electrons and holes are swept to opposite sides of the junction, respectively (such as ZnO/TiO$_2$ [10], and WS$_2$/MoS$_2$ [11]). The energy band of Z-scheme heterostructure is similar to type-II, and yet photogenerated electrons migrate from the conduction band (CB) of one side to the valence band (VB) of another

---

side (such as $CuBi_2O_4/WO_3$ [12], FeOCl/FeOOH [13]). The third is classical P-N heterojunction to prolong the life of electron-hole pairs (such as ZnO/GO [14]). The straddle-type (type-I) heterostructure refers to the VB and CB levels of one narrow-gap semiconductor interspersed within another wide-gap semiconductor. Under light irradiation, the electrons and holes flow to the same semiconductor, which is bad to separate electrons and holes. Thereby, researchers commonly believe that the straddle-type heterostructure is not considered favorable for separating photogenerated electron-hole [15–17].

Up to now, there is no research to prove that the straddle-type heterostructure has a role in promoting NIR photocatalysis, much less to explore the application of this type in photocatalytic sterilization for implant films. Nonetheless, studying thermally excited electrons and exploring photothermal-enhanced photocatalysis bring us a key revelation [18]. The electron transport properties of the heterogeneous interface may undergo essential changes under the addition of thermal effect [19]. Therefore, straddle-type heterostructure with a narrow-gap semiconductor may improve the NIR photocatalytic effect with photothermal conversion efficiency. Ag_2S is a black narrow-gap semiconductor with stable chemical properties, high electrical conductivity, and great biocompatibility [20,21]. The bandgap of Ag_2S is around 0.9

eV [16]. Ag_2S exhibits photocatalytic and photothermal responses under NIR excitation [22]. However, the narrow gap accelerates the complexation of photogenerated electrons and holes in Ag_2S, which greatly limits its NIR photocatalytic efficiency [22,23]. ZnS is a wide bandgap semiconductor commonly adopted photocatalyst for visible light [23,24]. Ag_2S and ZnS have good lattice matching due to the same transition metal sulfides. Particularly, the bandgap distribution satisfies the straddle-type heterostructure for Ag_2S and ZnS [16]. Therefore, the straddle-type heterostructure of ZnS/Ag_2S is expected to increase NIR photothermal-enhanced photocatalytic performance. Simultaneously, in the biomedical field, the locally elevated temperatures with NIR irradiation induce bacterial protein denaturation, damage bacterial membrane, and increase the permeability of bacterial membranes [25,26].

Herein, we constructed a ZnS/Ag_2S nanorod array films on the commonly used biomedical titanium implant, and the photocatalytic property and photocatalytic mechanism were explored. Expectantly, the straddle-type heterostructure of ZnS/Ag_2S exhibited excellent photothermal-enhanced photocatalytic properties under NIR irradiation. The photocatalysis mechanism of the straddle-type heterostructure was associated with NIR-induced electronic transport (Scheme 1a). As a verification of the proposed mechanism, we designed the ZnS/Bi_2S_3
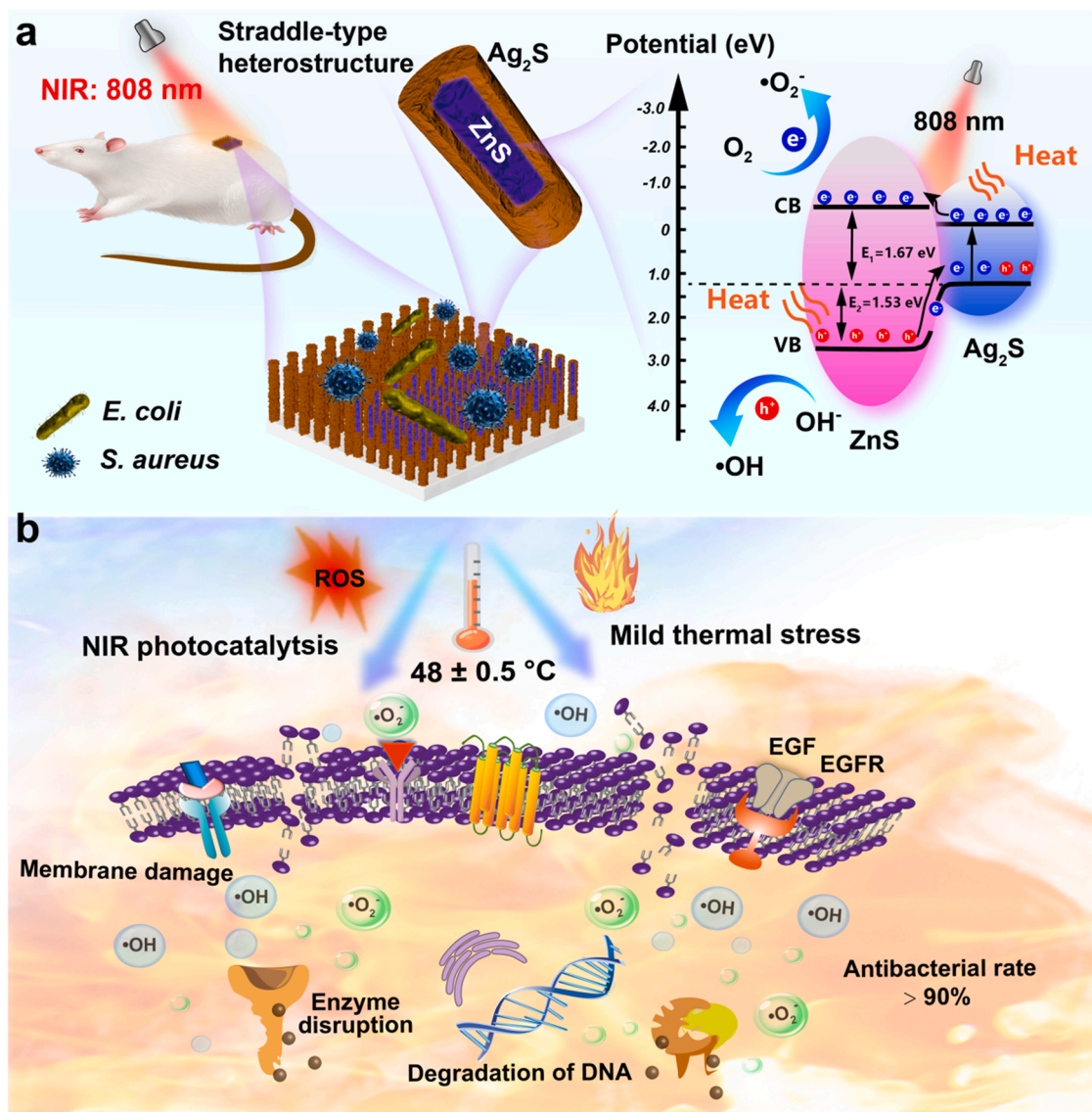
Scheme 1. Illustration of the NIR-triggered mild photothermal synergistic photocatalysis treatment of bacterial infections for ZnS/Ag_2S straddle-type heterostructure films.

heterostructure with the same straddle distribution of the energy band, and excitingly, its photocatalysis effect matched with the ZnS/Ag$_2$S heterostructure under NIR irradiation. Moreover, the mild photothermal synergistic photocatalysis of ZnS/Ag$_2$S heterojunction rapidly removed bacteria *in vitro* and *in vivo* (Scheme 1b). This work may provide valuable contributions to NIR photocatalysis based on straddle-type heterostructure, and show attractive prospects for mild photothermal synergistic photocatalysis treatment of bacterial infections on implant surfaces.

2. Experimental section

2.1. Preparation of ZnS nanorod arrays

The Ti plate (10 mm × 10 mm × 1 mm) was cleaned with ultrasound in HF and HNO$_3$ mixed solution. The volume ratio of HF, HNO$_3$, and ultrapure water was 1: 5: 34. Then wash it with alcohol and ultrapure water, respectively, and dry it for later use. Firstly, the ZnO seed layer was deposited on the Ti surface by atomic layer deposition (ALD, MNT-C-L3S1, Jiangsu MNT Micro and Nanotech Co., LTD, China) using diethyl zinc (DEZ, 99.999%, (C$_2$H$_5$)$_2$Zn) and H$_2$O as the precursors for zinc and oxygen, respectively. The specific process parameters were as follows: the temperature of the vacuum chamber was 150 ℃, the pulse times of DEZ and H$_2$O were 300 ms and 200 ms, respectively, and the N$_2$ purging time was 50 s. The reaction was repeated for 100 cycles to obtain the ZnO seed layer.

Afterward, the Ti with the seed layer was immersed in the growth solution mixing 0.025 M Zn(NO$_3$)$_2$•6 H$_2$O (AR, Aladdin, China) and 0.025 M hexamethylenetetramine (AR, C$_2$H$_{12}$N$_4$, Sinopharm, China), and hydrothermally treated at 90 ℃ for 4 h to synthesize ZnO nanorod array films. In a simple vulcanization process, the ZnO nanorod was entirely transformed into the ZnS nanorod. Briefly, the prepared ZnO has immersed in 3 g/L thioacetamide (TAA, > 99.0%, Sinopharm, China) aqueous solution and incubated at 60 ℃ for 17 h.

2.2. Preparation of ZnS/Ag$_2$S heterostructure nanorod arrays

Ag$_2$S as shell layer of ZnS/Ag$_2$S heterostructures partially transforming the surface of ZnS nanorods into Ag$_2$S by cation conversion. The Ag$_2$S shell structure was coated on the surface of ZnS by the cation conversion method. Compared with ZnS (K$_{sp}$ = 2.93 × 10^{-25}), the solubility product of Ag$_2$S (K$_{sp}$ = 6.69 × 10^{-50}) is much lower. The samples with various amounts of Ag$_2$S were prepared. In short, the samples with ZnS nanorod arrays were immersed in 0.0025 M AgNO$_3$ aqueous solution for 5 min, 10 min, 20 min, 40 min, and 80 min at 25 ± 1 ℃, respectively. The specimens were denoted as Zn/Ag-5, Zn/Ag-10, Zn/Ag-20, Zn/Ag-40, and Zn/Ag-80, respectively.

2.3. Materials Characterization

The prepared specimens were characterized by scanning electron microscopy (SEM, Magellan 400, FEI, USA), energy dispersive spectrometry (EDS, EPMA, JAX-8100, Japan), X-ray diffraction (XRD, Rigaku, Japan), and X-ray photoelectron spectroscopy (XPS, Thermo, PHI-5000, USA). Also, the microstructure of the coating was observed by transmission electron microscopy (TEM, JEM-2100 F, Japan). High-resolution TEM (HRTEM) images were recorded, and selected area electron diffraction patterns (SAED) were analyzed by the software Digtalmicrograph.

2.4. Photocatalytic and photocurrent tests

The degradation of methylene blue (MB) by the photocatalytic activity of the ZnS/Ag$_2$S heterostructure nanorod arrays was performed in an MB aqueous solution (4 ppm) under NIR irradiation. The samples were placed into 24-well plates with 1 mL of MB solution and then irradiated with 808 nm NIR (0.5 W cm^{-2}) for 20 min. The heat was generated in the process of NIR radiation. In order to peel off the effect of temperature on the catalytic performance, the temperature was cooled through the cooling water system to explore the NIR photocatalytic of the ZnS/Ag$_2$S heterostructure. The level of ROS generation at different intervals was evaluated with an enzyme labeling instrument (Bio Tek Cytation 5, USA) at 550–750.

Electron paramagnetic resonance spectrometer (EPR, Bruker, A300X-band, USA) was used to identify the species of ROS, and 5,5-dimethyl-1-pyrroline-N-oxide (DMPO, 50 mM) was used to trap hydroxyl radicals (•OH), and superoxide anion (•O$_2$), whereas 2,2,6,6-tetramethylpiperidine (TEMP, 50 mM) was adopted to investigate singlet oxygen (^{1}O$_2$). The NIR (0.8 W cm^{-2}) irradiation time was 5 min, 15 min, and 20 min, respectively.

The photo-electrochemical property of samples was detected in a standard three-electrode system and recorded on an electrochemical workstation (Metrohm, AUTO LAB PGSTAT128N). A saturated calomel electrode (SCE) was the reference electrode, a Pt plate was the counter electrode, and the work electrodes were the samples. The 0.2 M Na$_2$SO$_4$ aqueous solution was selected as the electrolyte. The irradiation sources were carried out on 808 nm NIR (0.8 W cm^{-2}), λ ≥ 400 nm (visible light, 300 W Xe lamp), and simulated sunlight (300 W Xe lamp), respectively.

2.5. In vitro antibacterial effects evaluation

2.5.1. Bacterial culture

Gram-negative bacteria *Escherichia coli* (*E. coli*, ATCC 25922) and Gram-positive strain of *Staphylococcus aureus* (*S. aureus*, ATCC 25923) were chosen to conduct *in vitro* bacterial experiments. Bacteria with a concentration of 5 × 10^6 CFU mL^{-1} in the logarithmic phase were used to evaluate the antibacterial ability of all samples. The bacteria were cultured at 37 °C with a constant temperature incubator. The samples were first placed in 24-well plates. The 500 μL bacterial suspension was sequentially moved into 24-well plates with examples.

2.5.2. Bacterial counting

The antibacterial abilities of various samples were tested *via* the platelet colony counting method. After cultivation for 6 h, the 24-well plates containing samples and the bacterial suspension were irradiated with or without the 808 nm NIR for 20 min. On the one hand, to explore the effect of NIR photocatalysis on antibacterial activity, a cooling water system was used to keep the samples with bacterial below 37 °C. The cooling water system excludes the effect of photothermal action on the antibacterial properties under NIR irradiation. On the other hand, without a cooling water system, the stable temperature of NIR irradiation (NIR, from 0.6 W cm^{-2} to 0.8 W cm^{-2}) was kept at 48 ± 0.5 ℃. The concentration of the bacteria solutions was diluted 100 times with 0.9 wt% NaCl solution. Then 100 μL bacterial suspensions were evenly daubed on an agar plate and re-cultured at 37 °C for 17 h. Finally, all culture plates were visualized by a digital camera. The corresponding antibacterial ratio was calculated as follows in Eq. (1).

$$\text{Antibacterial ratio (\%)} = (C - E)/C \times 100\% \qquad (1)$$

Where C was the average bacteria count in the control group (without NIR light), and E was the experimental group (with NIR light), respectively. The antibacterial rates thus calculated directly indicate the antibacterial effect of NIR irradiation, excluding the inhibition of the samples themselves.

2.5.3. Morphology of bacteria

The bacterial morphology of various samples was observed *via* the SEM (S3400N, HITACHI, Japan). After 6 h, the 24-well plates containing samples and the bacterial suspension were irradiated with or without the 808 nm NIR for 20 min. The method of with and without cooling was

the same as *Bacterial counting.* The bacteria were fixed for 4 h by 1 mL/well 2.5% glutaraldehyde solution (Sinopharm, China), and sequentially dehydrated *via* gradient alcohol (volume fraction: 30%, 50%, 75%, 90%, 95%, and 100%) for 10 min in turn.

2.5.4. Antibacterial ring test

The bacteriostatic ring test was used to evaluate the effect of ion release on antibacterial viability. Briefly, 200 μL of bacterial solution (1×10^7 CFU mL^{-1}) was first inoculated on the culture plate. Then the samples were placed on the agar plates in a face-to-face manner. After 17 h, the culture plate was photographed by a digital camera.

2.6. In vivo antibacterial effects evaluation

All animal procedures were performed following the Animal Management Rules of the Ministry of Health of the People's Republic of China and Guidelines for the Care and Use of Laboratory Animals of China. Sprague-Dawley rats (190–220 g) were employed to evaluate the *in vivo* antibacterial effects of ZnS/Ag$_2$S heterostructure. The rats were randomly separated into four groups, which were as follows: Ti (NIR-), Ti (NIR+), Zn/Ag-40 (NIR-), and Zn/Ag-40 (NIR+). The rats were anesthetized with 10% chloralhydrate (1 mL/100 g) by intraperitoneal injection. A 10 mm defection was created in the skin of the rat's back, and then samples were implanted to the left and right sides, respectively. 20 μL of bacteria (10^7 CFU/mL) were seeded on the sample surface. The NIR group was irradiated by NIR light at 0.8–1.0 W cm^{-2} for 15 min. Thermal imaging was used to monitor the temperature changes during the treatment process. The rats were euthanized at 1 and 4 days, and the surrounding tissues were evaluated by hematoxylin/eosin (H&E) and Giemsa staining. The primary organs of rats on 4 days were stained with H&E, assessing the bio-safety.

2.7. Cytocompatibility evaluation

2.7.1. Cell morphology

The cell inoculation density was 2×10^4 cells/well. After the cells were seeded on the samples for 1 day and 4 days. The samples were transferred to a new culture plate. The 2.5% glutaraldehyde solution was added at 4 °C for 12 h. Subsequently, dehydration was carried out as the 30%, 50%, 75%, 90%, 95%, and 100% ethanol/water solution, 10 min each time, and 100% ethanol dehydration twice. The surface was sprayed with platinum, and SEM observed the morphology of the cells.

2.7.2. Cell proliferation

The MC3T3-E1 at 2×10^4 cells/well concentration was used in the AlamerBlue evaluation. Briefly, the samples were placed in 24-well plates. After culturing for 1, 4, and 7 days, the growth medium was replaced by a 500 μL medium containing 10% (vol) AlamarBlue. After 2 h, the fluorescence intensity was measured at wavelength 560 nm (excitation) and 590 nm (emission).

2.7.3. Cell live/dead staining

Cells (5×10^4 cells/well) were cultured on the specimens for two days. Afterward, samples were rinsed with phosphate buffer solution (PBS) twice and added 100 μL of fluorescence dying solution (5 μM propidium iodide and 2 μM calcium-AM). After they were cultured for another 30 min, samples were washed with PBS and kept in PBS before being observed with a fluorescent microscope (OLYMPUS, DP72, Japan).

2.8. Statistical analysis

A GraphPad Prism statistical software conducted the values as the mean ± standard deviation (SD). The significant statistical difference was performed with a one-way analysis of variance (ANOVA). The *p*-value < 0.05 was regarded as statistically significant, and the *p*-value

was < 0.05, 0.01, and 0.001 were represented by "* ", "* *", and "* ** ", respectively.

3. Results and discussion

3.1. Characterization of ZnS/Ag$_2$S heterostructure films

Fig. 1a shows the preparation process of ZnS/Ag$_2$S nanorod array films. Firstly, the ZnO nanorods were prepared on the Ti surface by atomic layer deposition (ALD) and hydrothermal treatment (Fig. 1b). Then, the ZnO nanorods were transformed into ZnS nanorods by sulfidation treatment (Fig. 1c). The ZnS nanorods became thicker than ZnO nanorods, and showed a cylindrical shape with increased surface roughness (Fig. 1c), which associated with the Kirkendall effect caused by the difference in the diffusion rate of Zn^{2+} and S^{2-} [27]. As shown in Fig. 1d-f, ZnS/Ag$_2$S nanorod array films were synthesized by the mutual diffusion of Ag$^+$ (inward diffusion) and Zn^{2+} (outward diffusion) according to the solubility product of Ag$_2$S (K$_{sp}$ = 6.69 × 10^{-50}) and ZnS (K$_{sp}$ = 2.93 × 10^{-25}) [28]. The thickness of the Ag$_2$S shell can be accurately controlled by regulating the reactivity time. The diameter of the ZnS/Ag$_2$S nanorod decreased from 103.82 nm to 61.61 nm, and the thicknesses of all films remained essentially static (Fig. S1). The Ag content in the films was regulated by adjusting the Ag ion replacement time. Fig. 1g depicts the Ag content of ZnS/Ag$_2$S films increased, and the Zn content decreased with the silvering time. The contents of other elements (O, S, and Ti) in the film were similar (Table S1). The above results further verified the conversion process Zn^{2+} and Ag$^+$.

The surface elemental composition of ZnS, Zn/Ag-10, and Zn/Ag-40 was investigated by XPS, and the high-resolution XPS spectra were shown in Fig. 2a-c. The typical peaks of Ag3d$_{5/2}$ at 368.3 eV and Ag3d$_{3/2}$ at 374.3 eV were observed on all samples [28]. The Zn2p$_{3/2}$ and Zn2p$_{1/2}$ chemical states in ZnS were found at 1022.1 eV and 1045.2 eV (Fig. 2b) [29]. Meanwhile, the doublets of S2p with a separation of 1.1 eV were contributed by the Zn-S bond (S2p$_{3/2}$: 161.8 eV) and Ag-S bonds (S2p$_{1/2}$: 162.9 eV), as displayed in Fig. 2c [20]. In addition, Fig. S2 depicts the XPS full spectra of Zn/Ag-10 and Zn/Ag-40, which contained Ag, Zn, S, and a small number of C elements. In comparison, Zn, S, and C elements were detected on the ZnS films, which validated the EDS analysis well. The XPS results further verify the ZnS and Ag$_2$S phases in the heterojunction film.

The phase compositions of various samples were indicated by XRD (Fig. 2d). The characteristic peak at 28.6° of the ZnS sample corresponded to the (111) crystal plane of ZnS (ICDD #01–002–0564) [30]. As shown in the local magnification in Fig. 2d (red dotted frame), the diffraction peak intensity of ZnS was weak, indicating that ZnS primarily existed in the form of amorphous or nanocrystalline. The characteristic peak of the crystal plane of Ag$_2$S (34.7°) started to appear on Zn/Ag-10 [31,32], and the signal peak of ZnS disappeared. With increasing silvering time, the diffraction peaks of Ag$_2$S appeared at 26.3°, 28.9°, 31.5°, 33.6°, and 34.7° for both Zn/Ag-40 and Zn/Ag-80, corresponding to the (012), (111), (−112), (120), (−121) crystallographic planes of Ag$_2$S, respectively (ICDD #00011–0688). Accordingly, XRD result revealed that Ag$_2$S crystalline phase increased with treatment time. Raman spectra indicate that the peaks of LO and 2LO in ZnS samples were typical representatives of ZnS and, the characteristic peaks of ZnS were replaced by that of Ag$_2$S in Zn/Ag-40 (Fig. S3). Thereby, Raman spectra proved the successful construction of ZnS/Ag$_2$S heterostructure.

To further analyze the microstructure of ZnS/Ag$_2$S nanofilms, Zn/Ag-40 with an appropriate Ag$_2$S shell was selected for TEM analysis. The high-resolution TEM images demonstrated the ZnS/Ag$_2$S nanorod had a core-shell morphology (Fig. 2e), the core diameter was about 53.02 nm, and the shell thickness was approximately 29.42 nm. Selected area electron diffraction patterns (SAED) of A region (including core and shell) indicated a polycrystalline structure corresponding to the (012) and (−221) crystal planes of Ag$_2$S, and the (400) crystal plane of ZnS, respectively (Fig. 2e$_1$). As shown in Fig. 2e, the core (B region) and
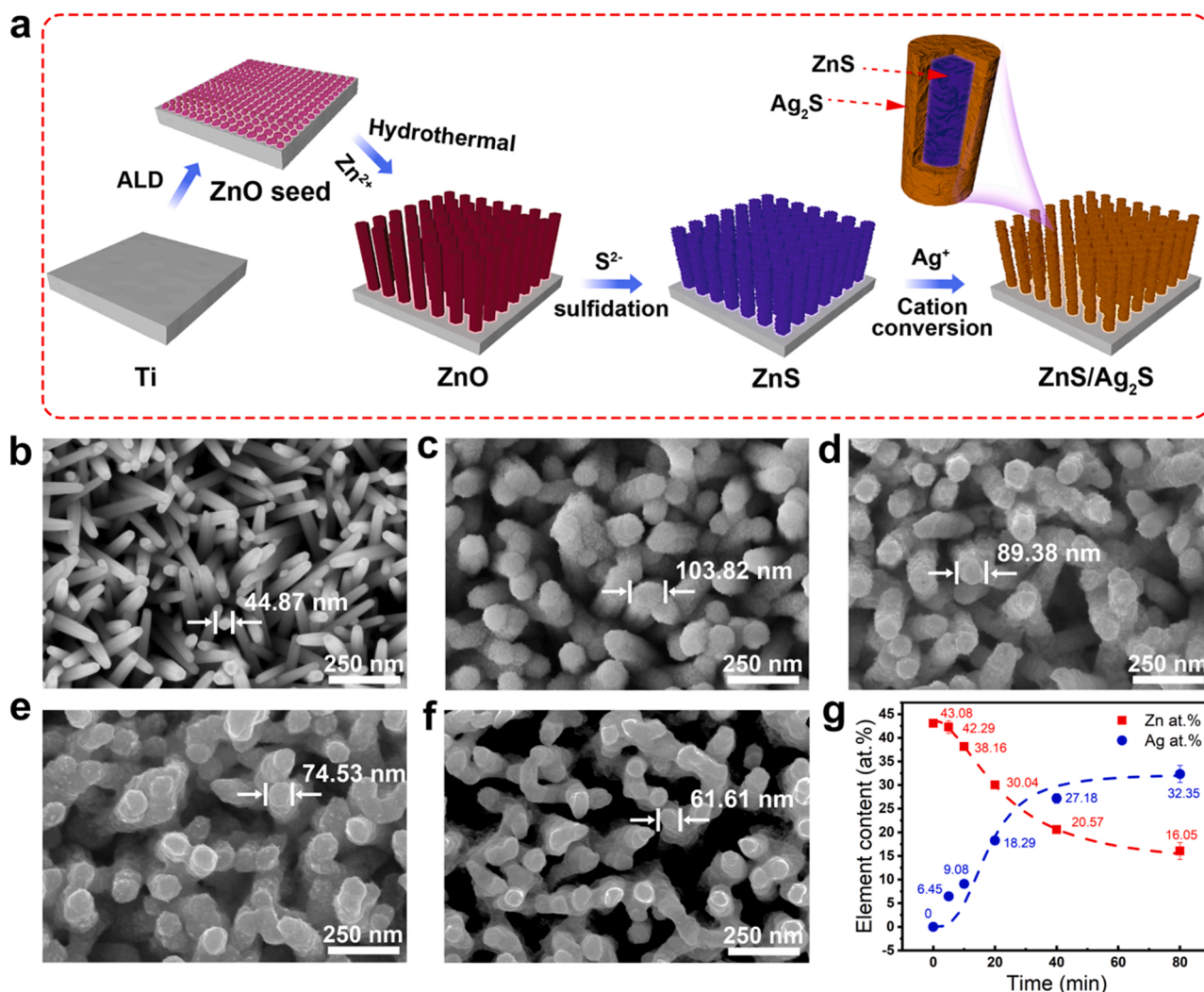
Fig. 1. Preparation and characterization of ZnS/Ag₂S heterostructure films. (a) Schematic illustration of synthesis process for the ZnS/Ag₂S core-shell heterostructure films on Ti surface. (b) SEM image of ZnO, (c) ZnS, (d) Zn/Ag-10, (e) Zn/Ag-40, and (f) Zn/Ag-80 samples. (g) The element content evolves with the time of cation conversion.

shell (C region) were selected for lattice fringe measurement. The interplanar spacing of the B region was 0.19 nm, which was identified as the (220) crystal plane of ZnS (Fig. 2e₂) [33]. The interplanar spacing of the C region was 0.31 nm, which corresponded to the (111) diffraction plane of Ag₂S (Fig. 2e₃). Further, the Fourier transform selected a more extensive range (20 nm × 20 nm) in the D region of the shell (Fig. 2e₄). The results showed that the D region was a typical Ag₂S single-crystal diffraction spot. As mentioned above, ZnS/Ag₂S core-shell heterostructure films were successfully prepared on Ti implant surface. And the Ag₂S shell thickness increased gradually. Meanwhile, the ZnS core diameter became progressively thinner with the treatment time. The optimal thicknesses of the ZnS core and Ag₂S shell layers were 49.83 nm and 32.65 nm, respectively.

3.2. NIR photocatalytic performance and mechanism

3.2.1. NIR photocatalytic performance

Light absorption at specific wavelengths is a premise for semiconductor photocatalysis. The UV–vis NIR spectra were obtained to uncover the light absorption of Ti (control group), ZnS, Zn/Ag-10, Zn/Ag-40, and Zn/Ag-80 (Fig. 3a). All ZnS/Ag₂S heterostructure films exhibit better absorption thresholds at 808 nm attachment than Ti and ZnS. As indicated by Fig. 3b, the bandgaps of ZnS, Zn/Ag-10, Zn/Ag-40,

and Zn/Ag-80 were estimated from the Tauc-plot by Kubelka-Munk method (Eq. 2):

$$(\alpha h v)^{1/n} = A(h v - E_g) \qquad (2)$$

Where α is the absorption index, h is Planck's constant, and v is the frequency. A is the constant, and E_g represents the bandgap of semiconductors. Both ZnS and Ag₂S are direct bandgap semiconductors, n = 1/2. After calculation, the E_g of ZnS, Zn/Ag-10, Zn/Ag-40, and Zn/Ag-80 were 3.20 eV, 1.68 eV, 1.42 eV, and 1.13 eV (ZnS > Zn/Ag-10 > Zn/Ag-40 > Zn/Ag-80). With the increase of Ag₂S content, the E_g of ZnS/Ag₂S heterostructure gradually decreased, and the E_g of Zn/Ag-80 (1.13 eV) approached pure Ag₂S (0.9–0.95 eV). It suggests that the thickness of the Ag₂S shell gradually increases and becomes the primary light absorption body.

The photoelectric conversion ability of materials indirectly reflects their photocatalytic performance. Photoelectric testing is a reliable method to investigate photocatalytic efficiency. Therefore, the transient photocurrent responses of samples under NIR irradiation are detected. Interestingly, as shown in Fig. 3c, the Zn/Ag-10, Zn/Ag-40, and Zn/Ag-80 samples had obvious photocurrent under NIR irradiation. The photocurrent of Zn/Ag-40 was significantly higher than that of Zn/Ag-10 and Zn/Ag-80 (about five times). The order is Zn/Ag-40 > Zn/Ag-80 > Zn/Ag-10 > ZnS > Ti. With the increase of Ag₂S content, the PL
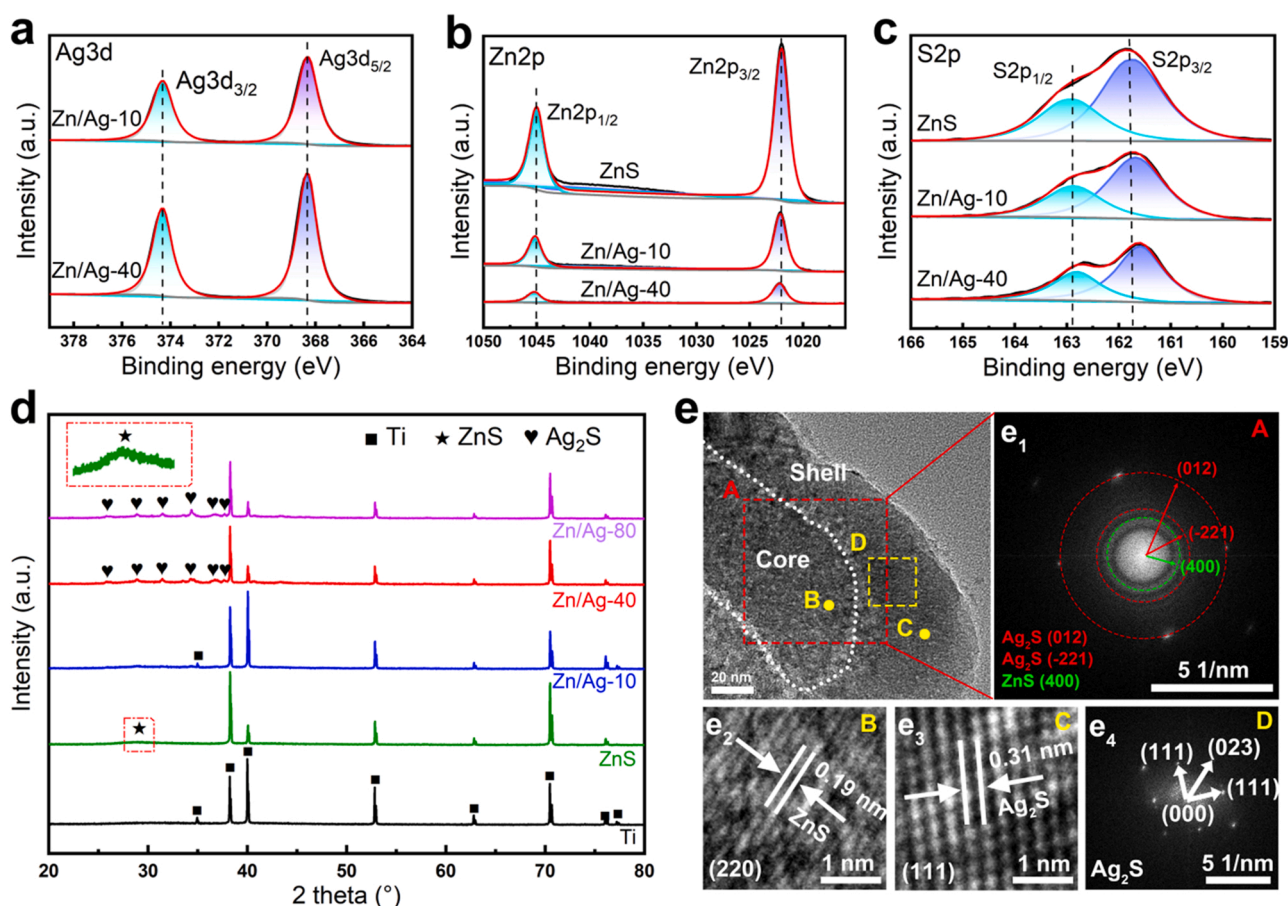
Fig. 2. Characterization of ZnS/Ag$_2$S heterostructure films. (a) The XPS spectra of Ag3d high-resolution of Zn/Ag-10 and Zn/Ag-40, respectively. (b) XPS spectra of Zn2p and (c) S2p high resolution of ZnS, Zn/Ag-10, and Zn/Ag-40, respectively. (d) XRD patterns of the various samples. (e) HRTEM images of Zn/Ag-40 and SAED (e$_1$: A region in Fig. 1e and e$_4$: D region in Fig. 1e) and corresponding lattice spacing calibration (e$_2$: B region in Fig. 1e, e$_3$: C region in Fig. 1e).

peak intensity of ZnS/Ag$_2$S heterostructure films decreased and then increased. The peak intensity of Zn/Ag-40 decreased to the lowest (Fig. S4). This result denotes that Zn/Ag-40 had a fast NIR-responsive ability and a low recombination rate of electron-hole pair. Zn/Ag-40 was heated and cooled continuously for five cycles to examine the sustainability of photothermal conversion, and no performance decline was detected [34]. Surprisingly, the photoelectric conversion performance was opposed when visible light (Fig. 3d) and simulated sunlight (Fig. S5) were utilized. The order of photocurrent intensity was ZnS > Zn/Ag-10 > Zn/Ag-40 > Zn/Ag-80 > Ti. Compared with previous research [35,36], the results contradict the belief that ZnS/Ag$_2$S open structural (Ag$_2$S nanoparticle compounded on the surface of ZnS) heterostructure benefits. Potentially, there is a new photoelectric conversion mechanism for the ZnS/Ag$_2$S core-shell heterostructure in this paper. The details will be introduced below.

The Ag$_2$S with narrow gaps has excellent photothermal conversion ability, and the thermal could also enhance the photocatalysis effect [37]. The photothermal temperature curves (Fig. 3e) and thermal-imaging pictures (Fig. S6a) show the surface temperature of Ti, ZnS, Zn/Ag-10, Zn/Ag-40, and Zn/Ag-80 gradually increased. The temperature of Ti and ZnS rose to 48 °C and 52.3 °C after 20 min of irradiation, respectively. In comparison, the temperatures of Zn/Ag-10, Zn/Ag-40, and Zn/Ag-80 increased by 57.9 °C, 59.5 °C, and 59.5 °C, respectively, significantly higher than that of Ti and ZnS. All ZnS/Ag$_2$S heterostructure films had excellent photothermal conversion efficiency, switching responses, and stability (Fig. S6b). MB can be faded by potent oxidizing ROS, which was used to evaluate photocatalytic ROS production (Eq. 3).
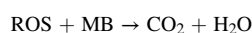
$$ROS + MB \rightarrow CO_2 + H_2O \tag{3}$$

Fig. 3 f shows the degradation behaviors of MB for Ti, ZnS, Zn/Ag-10, Zn/Ag-40, and Zn/Ag-80 after NIR irradiation for 20 min. The results showed that the photocatalytic ability of the ZnS/Ag$_2$S heterostructure first increased and then decreased with the increase of Ag$_2$S content. The photocatalytic ability of Zn/Ag-40 was the strongest. Because the black ZnS/Ag$_2$S heterostructure films had photothermal conversion ability, we carried out thermal stripping of Zn/Ag-40 to further investigate the effect of thermal-concomitant on photocatalytic ability (Fig. 3 g). After excluding the thermal influence, the temperature was kept below 37 °C (Fig. S7 shows corresponding temperature curves), the degradation rate of MB decreased significantly at different irradiation time points. It meant that the thermal-concomitant of ZnS/Ag$_2$S heterostructure promoted photocatalytic ability under NIR irradiation [38].

Electron paramagnetic resonance (EPR) was used to identify the photocatalytic ROS species of the Zn/Ag-40 heterostructure (Fig. 3h-j). The 5,5-dimethyl-1-pyro-line-N-oxide (DMPO) was employed to confirm hydroxyl radical (•OH) and •O$_2^-$ generation. The EPR signals of ZnS/Ag$_2$S heterostructure in DMPO identified a 1: 2: 2: 1 quartet signal characteristic (Fig. 3 h), indicating that Zn/Ag-40 heterostructure can generate •OH under NIR irradiation. In addition, the ZnS/Ag$_2$S heterostructure manifested the clear signals of •O$_2^-$ (Fig. 3i). Meanwhile, with the increase of NIR irradiation time, the EPR signal intensity of •OH and •O$_2^-$ increased gradually, suggesting that more •OH and •O$_2^-$ were produced. The ^{1}O$_2$ signal of the Zn/Ag-40 in EPR was trapped by 4-amino-2,2,6,6-tetramethyl piperidine (TEMP). The ^{1}O$_2$ was not produced after
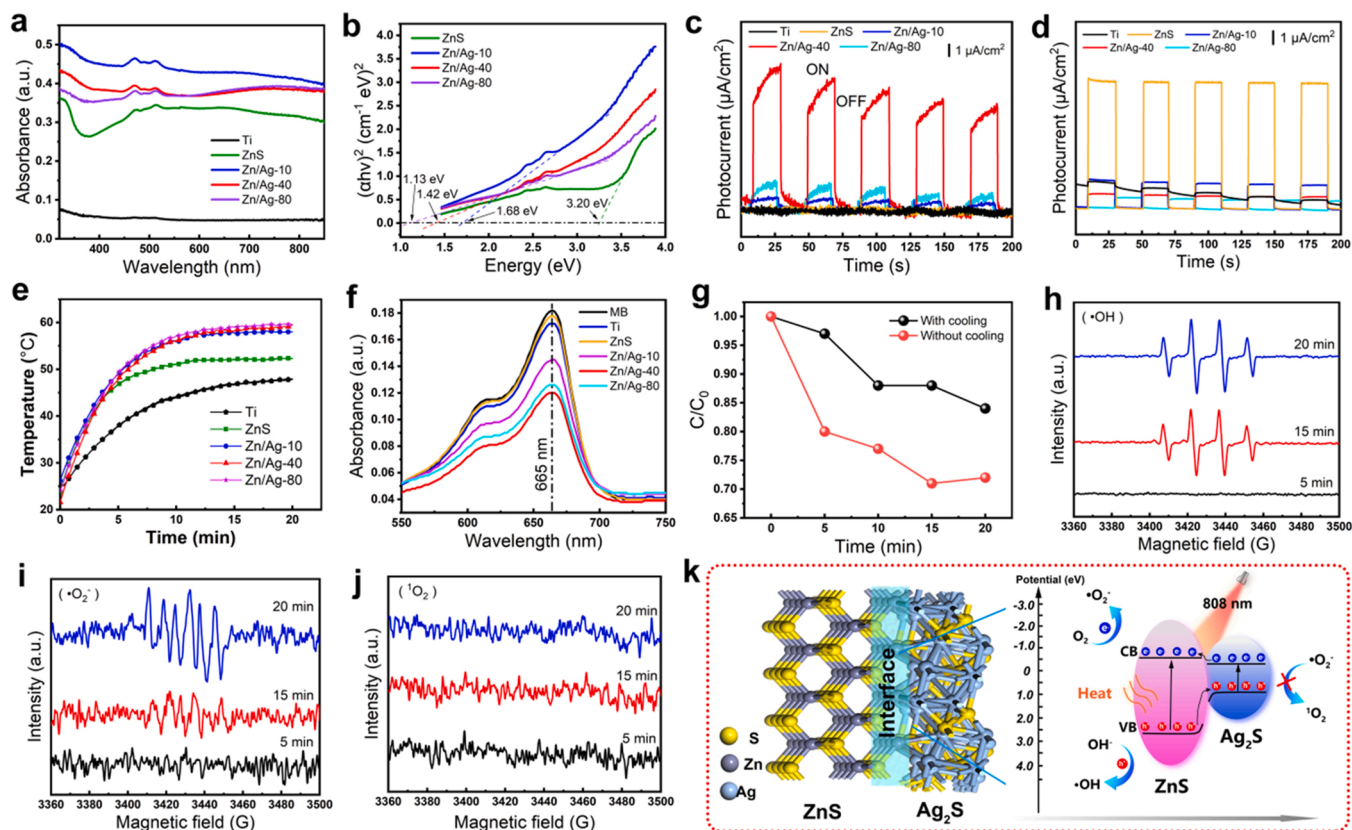
Fig. 3. Photocatalytic and photocurrent effects of the samples. (a) The UV–vis NIR absorption spectra and (b) Tauc plot from the UV–vis absorption spectra of the samples. Transient photocurrents under (c) NIR and (d) visible light for the different samples. (e) The photothermal curves of the different samples under NIR irradiation. (f) Photocatalytic activity from MB (control) and samples exposed to NIR. (g) Photocatalytic activity from Zn/Ag-40 under NIR irradiation, with and without cooling. (h-j) EPR spectra Zn/Ag-40 for detection of (h) •OH, (i) •O$_2^-$, and (j) ^{1}O$_2$ at different times. (k) Schematic depictions of photocatalytic of ZnS/Ag$_2$S heterostructure.

irradiating various times (Fig. 3j). The fluorescence quenching results of dihydroethidium (DHE) revealed that •O$_2^-$ generated by Zn/Ag-40 NIR photocatalysis could effectively quench DHE (Fig. S8a). Moreover, the degradation of MB was significantly reduced by the addition of C$_3$H$_8$O to consume the •OH generated by NIR photocatalysis (Fig. S8b). These results suggest that the ZnS/Ag$_2$S heterostructure photocatalytic ROS species include •O$_2^-$ and •OH, further supporting the EPR analysis. The schematic diagram of the mechanism shown in Fig. 3k clarified that the NIR photocatalytic performance and photoelectric conversion effect of the ZnS/Ag$_2$S heterostructure mainly benefited from the practical separation of e$^-$ and h$^+$ at the hetero-interface. Immediately, O$_2$ and OH$^-$ reacted with higher lifetime e$^-$ and h$^+$ to form ROS (•OH and •O$_2^-$), respectively [39]. The •O$_2^-$ failed to obtain further h$^+$ to form ^{1}O$_2$.

3.2.2. Density functional theory (DFT) theoretical calculations

In order to further explore the heterostructure photocatalytic mechanism, the structural properties of composites and the interfacial interaction between the ZnS and Ag$_2$S phases were investigated by DFT calculations. As shown in Fig. 4a, the crystal structures of ZnS and Ag$_2$S were optimized and matched to form a ZnS/Ag$_2$S heterostructure. The density of states (DOS) and the degree of the orbital contribution of ZnS/Ag$_2$S heterostructure were investigated for electron transfer characteristics. The energy gap diagram of Fig. 4b noted that the bandgap of the ZnS/Ag$_2$S heterostructure was 1.03 eV, which was close to the experimental results. The total density of state (TDOS) (Fig. 4c) illustrated that the contribution of the valence band (VB) originated mainly from the p-d hybridized, and the conduction band (CB) consisted mainly of p orbitals. The project density of state (PDOS) (Fig. 4d-f) showed that the VB was mainly derived from the Ag-d of Ag$_2$S, while the CB was mainly

derived from the Zn-p of ZnS, Ag-p of Ag$_2$S, and S-p (ZnS and Ag$_2$S). Therefore, under NIR light irradiation, the electrons would jump from Ag-d of Ag$_2$S to Ag-p of Ag$_2$S. Moreover, some of the electrons would further leap to Zn-p of ZnS. These results suggested that the photogenerated electrons in Ag$_2$S were rapidly guided by ZnS during the photocatalytic process and thus flowed to the ZnS, which extended the lifetime of the photogenerated electrons, thereby enhancing the photocatalytic performance of the heterostructure.

3.2.3. Mechanism of NIR photocatalysis

As well known, the UPS spectrum can show the electronic structure of the valence band. It allows determining the two main electronic parameters, the work function (W$_s$ = 21.22 − E$_{cut-off}$, E$_{cut-off}$ is a secondary cut-off edge) and the Fermi level position concerning the valence band maximum (E$_{VBM}$ = E$_f$ − VB) [39]. The work function (W$_s$) is the minimum energy required for an electron to escape from the material interior to the surface. Thus, the relationship between the Fermi level and the work function is expressed as W$_s$ = E$_{AVE}$ - E$_f$. The energy band levels of ZnS, Ag$_2$S (Zn/Ag-80), and Zn/Ag-40 were evaluated by UPS (Fig. 5a-f). By applying the linear approximation method to the UPS spectra, the work functions of ZnS, Ag$_2$S, and Zn/Ag-40 were estimated to be 4.09 eV, 4.97 eV, and 4.79 eV, respectively. Namely, the corresponding Fermi levels were − 4.09 eV, − 4.97 eV, and − 4.79 eV, respectively. By calculation, the VB of ZnS, Ag$_2$S, and Zn/Ag-40 were − 6.52 eV, − 5.87 eV, and − 5.61 eV, respectively. The quantities previously determined are as the vacuum level. Therefore, according to the relationship between the potential of the normal hydrogen electrode (E$_{NHE}$) and the energy of the vacuum (E$_{AVE}$), E$_{NHE}$ = -(E$_{AVE}$ + 4.44) eV (at 298 K), the VB of ZnS, Ag$_2$S, and ZnS/Ag-40 were poised at 2.08 eV,
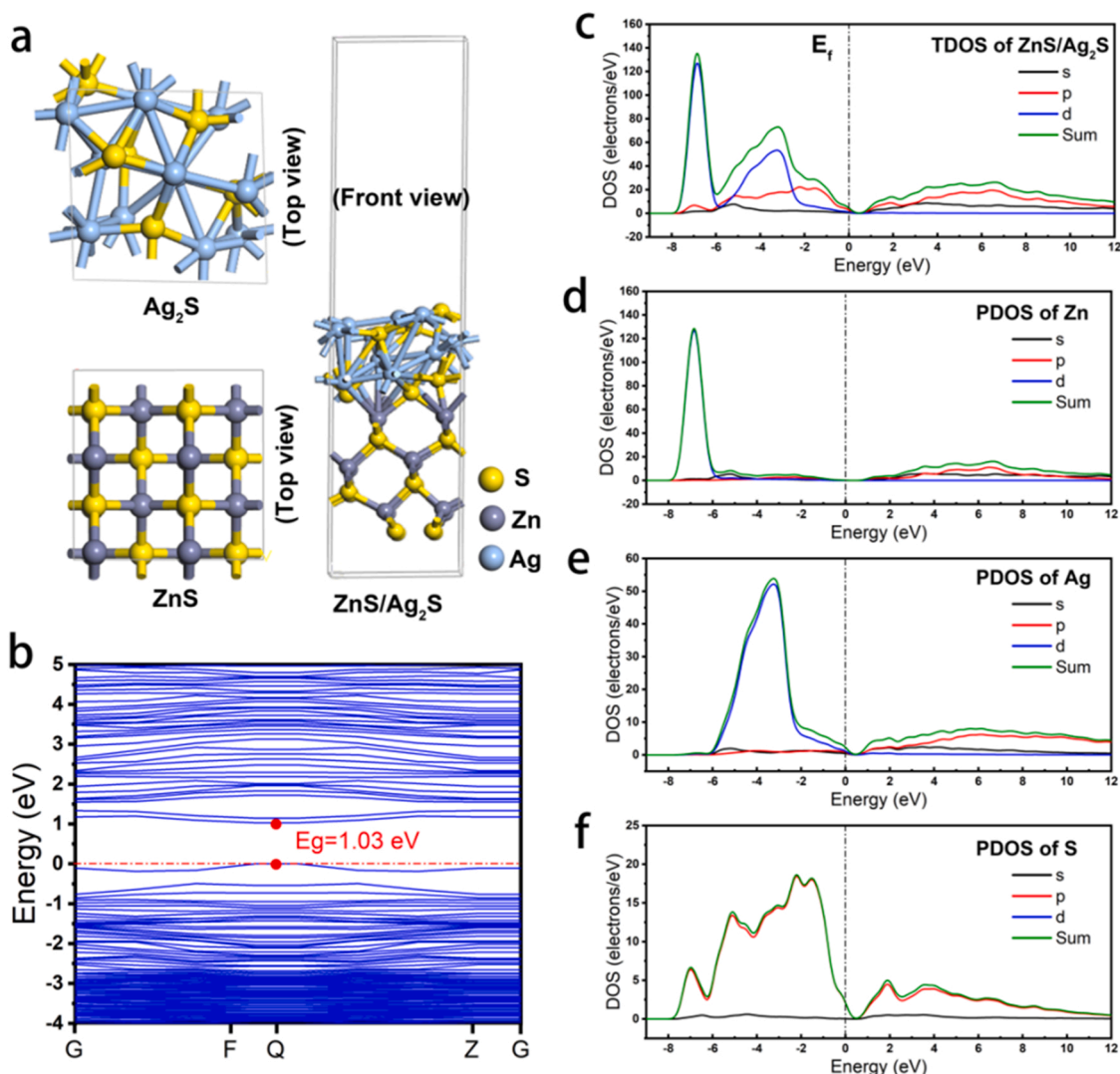
Fig. 4. DFT calculations of ZnS/Ag₂S heterostructure. (a) Structure optimization models of ZnS (110), Ag₂S (111), and ZnS/Ag₂S heterostructure for different perspectives. (b) The band structure of ZnS/Ag₂S heterojunction. Theoretical calculations of (c) TDOS and (d-f) PDOS of ZnS/Ag₂S heterojunction.

1.43 eV, and 1.17 eV, respectively. Table 1 summarizes the values of W_s and E_f. Based on the above study of the component, bandgap, and physicochemical properties, Zn/Ag-80 was approximated as Ag₂S. So here, the bandgap of Ag₂S nanorod films was 1.13 eV, and ZnS was 3.20 eV (Fig. 3b). As we know, ZnS and Ag₂S shared a Fermi level after ZnS contact with Ag₂S. The VB and CB levels of the ZnS component were shifted downward by 0.7 eV, and the VB and CB positions were 2.78 eV (*Vs. NHE*) and −0.42 eV (*Vs. NHE*), respectively. The VB and CB levels of Ag₂S were shifted upward by 0.18 eV, and the VB and CB positions were 1.25 eV (*Vs NHE*) and 0.12 eV (*Vs. NHE*), respectively. A schematic diagram of the band distribution was drawn in Fig. 5a.

According to literature research [12,15,39,40], existing theories do not support separating photogenerated electron-hole pairs for straddle-type heterostructure. Therefore, the photocatalytic mechanism of straddle-type heterostructure is worth thinking about profoundly. Fig. 5g displays the schematic diagram of ZnS/Ag₂S heterostructure for open structure (other work) and core-shell stricture (this work), then discusses the electron transfer mechanism. In previous reports, the ZnS/Ag₂S heterostructure is mainly used in solar photocatalysis of nanomaterials. The holes and electrons are generated under the excitation of sunlight, and the excited electrons in the ZnS conduction band (CB) are injected into the CB of Ag₂S to achieve electron-hole pair separation. In this work, the bandgap of Ag₂S (1.12 eV) was much lower

than that of NIR (1.53 eV) [41]. After NIR irradiated the Ag₂S shell, the VB electrons were excited and then transitioned to the CB of Ag₂S. We know the energy band $E_1 = 1.67$ eV from VB of Ag₂S to CB of ZnS, beyond the 0.14 eV compared to NIR. Nevertheless, ZnS/Ag₂S heterostructure films illustrated excellent photothermal conversion efficiency (Fig. 3e) and switching stability (Fig. S6b), which provided a certain number of hot electrons and energy. Thereby, the electrons in the VB of Ag₂S overcame the energy barrier and transitioned to the CB of ZnS. The DFT calculations investigated this process of electron transfer (Fig. 4). What was critical was that the bandgap from VB to ZnS to VB of Ag₂S was $E_2 = 1.53$ eV. Thus, the electrons from VB of ZnS jumped to the VB of Ag₂S under NIR irradiation. Simultaneously, the thermal radiation coupled with the photon energy enhanced the electrons jumping ability. This process prolonged the lifetime of electrons, and the CB of ZnS (−0.42 eV, *Vs. NHE*) was more negative than that of O₂/•O₂⁻ (−0.33 eV, *Vs NHE*) [41]. Therefore, Eq. 4 process was shown to generate •O₂⁻ (Fig. 3i). In addition, OH⁻ combined with the holes left by the VB of ZnS based on the electron transfer mechanism [34]. Namely, OH⁻ was oxidized to •OH (Eq. 5), which perfectly matched the ROS determination results (Fig. 3 h).
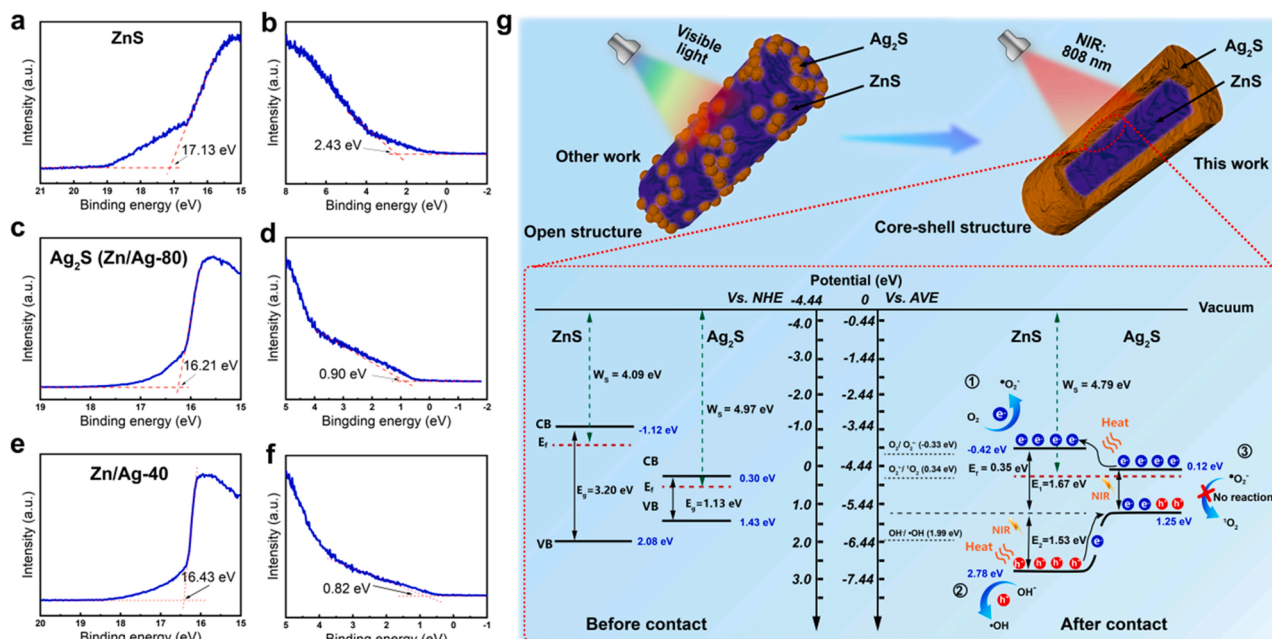
$$O_2 + e^- \rightarrow \bullet O_2^- \tag{4}$$

$$OH^- + h^+ \rightarrow \bullet OH \tag{5}$$

Fig. 5. Mechanism of NIR photocatalytic for straddle-heterostructure. UPS spectra, the binding energy of the secondary cut-off edges ($E_{cut-off}$), and Fermi level position concerning valence band maximum (E_{VBM}) for (a, b) ZnS, (c, d) Ag$_2$S (Zn/Ag-80), and (e, f) Zn/Ag-40. (g) The mechanism diagram of NIR photocatalytic for ZnS/Ag$_2$S heterostructure.

Table 1
The values of W_s and E_f of ZnS, Ag$_2$S, and Zn/Ag-40.

Sample	W_s (eV, Vs. AVE)	E_f (eV, Vs. NHE)	E_f – VB (eV)
ZnS	4.09	-0.35	2.43
Ag$_2$S	4.97	0.53	0.90
Zn/Ag-40	4.79	0.35	0.82

$$\bullet O_2^- + h^+ \rightarrow {}^1O_2 \qquad (6)$$

As displayed in Fig. 5g, after the contact between ZnS and Ag$_2$S, an internal electric field (IEF) is formed at the heterojunction interface, which is mainly caused by the different Fermi energy levels of ZnS and Ag$_2$S [42,43]. The excited electrons of ZnS combined with the holes left after the electron transition of Ag$_2$S. The VB of Ag$_2$S acted as a recombination platform for photogenerated electrons and holes when leaving more substantial reduction/oxidation potentials of separated electrons and holes on the VB of ZnS and the CB of Ag$_2$S. Therefore, the reaction of Eq. (6) did not occur even if the $\bullet O_2^-/^1O_2$ energy level was located above the VB of Ag$_2$S (Fig. 3j). According to the above electron transfer mechanism of the ZnS/Ag$_2$S straddle-type heterostructure, high-energy visible light excited the electrons in the VB of ZnS to transition to the CB of ZnS, inhibiting the secondary transition of Ag$_2$S electrons to the CB of ZnS. The electron-hole pairs were hardly effectively separated, and the photocatalytic efficiency was depleted. Therefore, the open structure (other work) is suitable for photocatalysis of visible light/simulated sunlight, while the straddle-type heterostructure of the core-shell design (this work) has a specific NIR photocatalytic mechanism.

Based on the electron transfer mechanism of the above straddle-type heterostructure, ZnS/Bi$_2$S$_3$ straddle-type heterostructure was designed to support and demonstrate the inquiry (Fig. 6a) [16]. The supporting information showed the preparation process, morphology, component, and phase of the ZnS/Bi$_2$S$_3$ heterostructure (Figs. S9-S11). We characterized the photocatalytic, photothermal, and photoelectric properties of the ZnS/Bi$_2$S$_3$ heterostructure films. Similar to the ZnS/Ag$_2$S heterojunction, the photocatalytic (Fig. 6b) and photothermal (Fig. 6c) properties of the ZnS/Bi$_2$S$_3$ heterostructure increased and then

decreased with increasing Bi$_2$S$_3$ content, and Zn/Bi-40 showed the best photocatalytic and photothermal effect. In addition, Zn/Bi-40 demonstrated the highest photocurrent intensity under NIR light (Fig. 6d). In contrast, photocurrent intensity became lower with the loading of Bi$_2$S$_3$ under visible light (Fig. 6e) and simulated sunlight (Fig. 6f). This result strongly supported the straddle-type heterostructure to promote the behavior of NIR photocatalysis, which perfectly agrees with the electron transfer mechanism in Fig. 5g.

The prepared ZnS/Ag$_2$S and ZnS/Bi$_2$S$_3$ heterostructure films illustrated the potential of straddle-type heterojunctions in enhancing NIR photocatalysis. The efficient application of NIR is a long-standing expectation in the photocatalytic field. This study complements the theory of heterostructures and provides theoretical guidance for the design of photocatalytic systems, which may also provide a particular incentive to make valuable contributions to the nanomaterial systems in photocatalysis.

3.3. Antibacterial activity in vitro

ZnS/Ag$_2$S heterostructure film produces the photothermal effect under NIR irradiation. A cooling system was created to display only photocatalysis-mediated antibacterial without the thermal effect. The temperature was kept below 37 °C when NIR therapy, corresponding temperature curves are shown in Fig. S12. The antibacterial activity of ZnS/Ag$_2$S heterostructure against *E. coli* and *S. aureus* was evaluated in Fig. 7a-d. Neither Ti nor ZnS exhibited any antimicrobial effect compared to the samples without NIR exposure. On the contrary, many bacteria died after Zn/Ag-10 and Zn/Ag-40 were exposed to NIR for 20 min. The antibacterial rates of Zn/Ag-10 and Zn/Ag-40 against *E. coli* were 70.38% and 88.47%, respectively (Fig. 7b). The antibacterial rates of Zn/Ag-10 and Zn/Ag-40 against *S. aureus* were 84.16% and 87.97%, respectively (Fig. 7d). This result demonstrated that the ZnS/Ag$_2$S heterostructure had a specific photocatalytic sterilization ability. Simultaneously, the antibacterial rate of Zn/Ag-40 was higher than that of Zn/Ag-10, which further suggested that the stronger the photocatalytic ability of the ZnS/Ag$_2$S heterostructure, the better the photocatalytic sterilization effect.

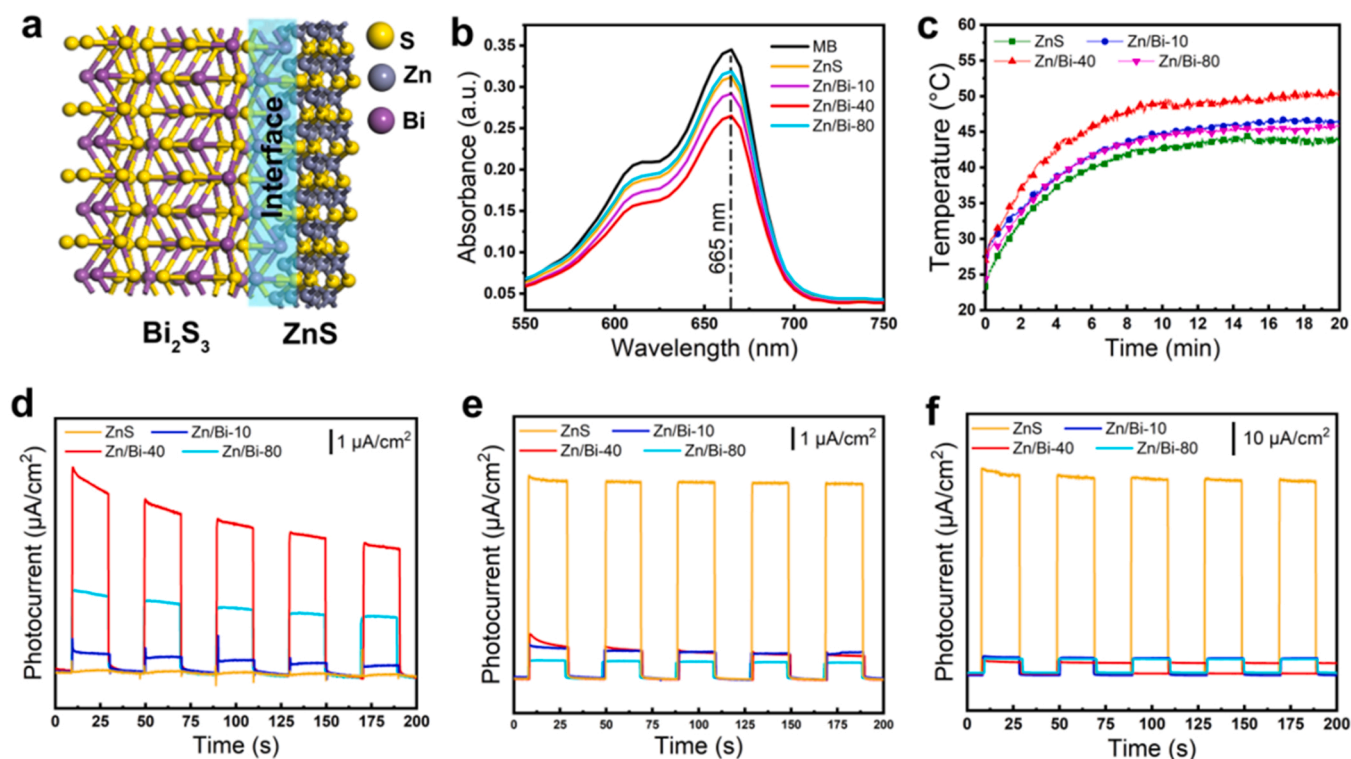The SEM morphologies of *E. coli* and *S. aureus* with and without NIR

Fig. 6. Photocatalytic, photothermal, and photoelectric properties of the ZnS/Bi$_2$S$_3$ heterostructure. (a) Schematic diagram of ZnS/Bi$_2$S$_3$ heterostructure. (b) Photocatalytic activity from MB (control) and various samples exposed to NIR. (c) The photothermal curves of the different samples under NIR irradiation. Transient photocurrents of (d) NIR irradiation, (e) visible light, and (f) simulated sunlight for different samples.

irradiation were observed to reveal the antibacterial activity of ZnS/Ag$_2$S heterostructure films. The temperature of samples was kept below 37 °C under NIR irradiation, corresponding temperature curves are exhibited in Fig. S13. As Fig. 7e, f, the surfaces of *E. coli* (rod shape) and *S. aureus* (spherical shape) were morphologically intact in the dark. Bacteria had smooth surfaces with no apparent antibacterial activity. In particular, some tentacles (blue arrows) were between the bacteria on the Ti surface, which was conducive to "communication". After NIR irradiation for 20 min, the *E. coli* and *S. aureus* on Ti and ZnS surfaces were intact. In sharp contrast, *E. coli* and *S. aureus* cultured on the surfaces of Zn/Ag-10 and Zn/Ag-40 have distinct degrees of metamorphosis (red arrows). The bacterial membrane was damaged, and the intracellular protein flowed out.

The mild photothermal-enhanced (48 ± 0.5 °C) photocatalytic antibacterial ability of Zn/Ag-40 was characterized. Excessive temperature kills bacteria while burning physiological tissues. So, it was essential to keep bacteria in heat stress at a mild temperature [44]. The mild injury caused by the microenvironment at 48 °C for a short time (about 15–20 min) can be recovered quickly [44–46]. Thus, 48 °C was chosen for the antibacterial experiments (Fig. 8b, d). Fig. 8a indicated that ZnS/Ag$_2$S heterostructure exhibited excellent antibacterial activity against *E. coli* and *S. aureus* under NIR irradiation. The antibacterial rates of *E. coli* and *S. aureus* reached 99.31% and 93.97%, respectively, achieving the quick removing bacteria on the Ti implant surface (Fig. 8e). Comparing the morphologies of bacteria before and after NIR irradiation, bacteria irradiated had severe membrane damage (blue arrow) and a large amount of protein leakage (red arrow) (Fig. 8c). In order to determine the bacteriostatic effect of the ion release on bacteria, a bacteriostatic ring experiment was carried out. As seen in Fig. 8 f, no significant antibacterial regions existed around the samples. Thus, the ion-releasing antibacterial of ZnS/Ag$_2$S heterogeneous films was not the primary factor for rapidly removing bacteria.

Based on the above results and discussion, the antibacterial mechanism of mild photothermal-enhanced photocatalysis of ZnS/Ag$_2$S

heterostructure films was described in Fig. 8 g. The ZnS/Ag$_2$S heterostructure received a large amount of ROS (hydroxyl radical and superoxide anion) after NIR irradiation. As a highly oxidative substance, ROS destroys a variety of bacterial biomolecules, such as enzyme disruption [47], membrane damage [40], denaturation of proteins [48], and DNA degradation [49]. Moreover, the photocatalytic effect of the ZnS/Ag$_2$S heterostructure was significantly enhanced under the action of heat (Fig. 3 g) [18]. In turn, the photocatalytic antibacterial efficiency was improved. Particularly, the photothermal environment put bacteria in a stress state and increased the membrane's permeability, which enhanced the killing effect of ROS on bacteria.

3.4. Antibacterial activity in vivo

A rat model of subcutaneous infection was built to confirm the *in vivo* antibacterial function of ZnS/Ag$_2$S heterostructure under NIR irradiation. Briefly, the rats were randomly divided into four groups (Ti (NIR-), Ti (NIR+), Zn/Ag-40 (NIR-), and Zn/Ag-40 (NIR+)). After samples with bacteria were implanted on the back of rats, NIR light was used to irradiate the sample implantation site for 15 min to remove the bacteria rapidly (Fig. 9a). After 1 and 4 days of treatment, the *in vivo* samples of rats were analyzed by smear plate. The results showed that Ti (NIR+) had no antibacterial ability, while Zn/Ag-40 (NIR+) exhibited excellent antibacterial effects (Fig. 9c). The quantitative statistics showed that the antibacterial rates of Zn/Ag-40 (NIR+) were 94.36% and 90.89%, respectively (Fig. 9b). This result matched the *in vitro* antibacterial evaluation. Fig. 9d shows the temperature change curves and Fig. 9e exhibits the temperature distribution map of rats. It is noteworthy that although the rats were irradiated with NIR for 15 min, the Zn/Ag-40 (NIR+) group remained at 48 °C for only about 9 min. The rat skins of the Zn/Ag-40 (NIR+) group in Fig. S14 had an intact epidermis and clear hair follicle structure. Thereby, the practice of a mild photothermal strategy was safe *in vivo*.

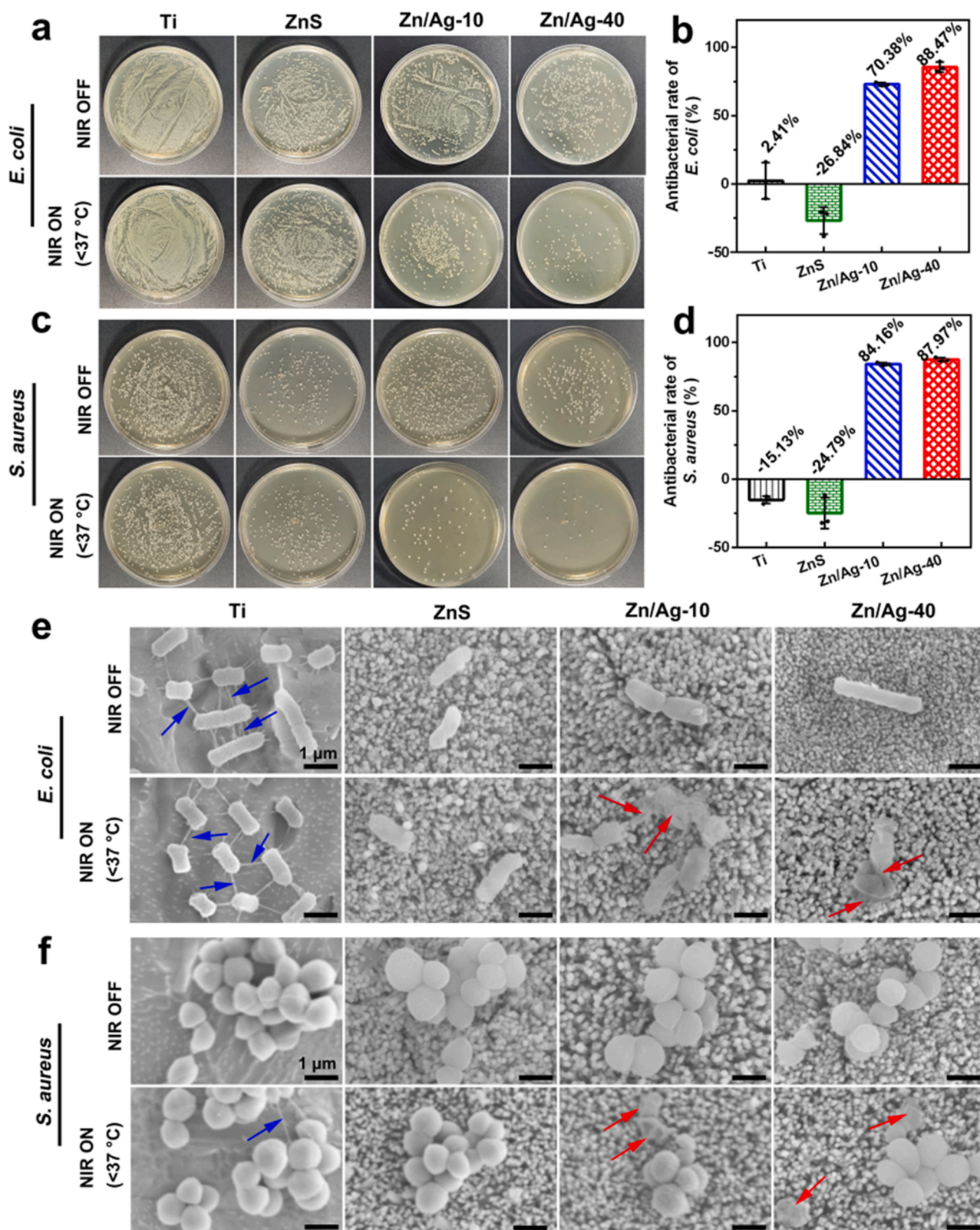H&E staining (Fig. 9f) and Giemsa staining (Fig. 9g) were executed to

Fig. 7. *In vitro* antibacterial investigation of ROS upon NIR irradiation with cooling. (a) Photographs of cultivated *E. coli* on agar plates and (b) corresponding antibacterial rates of *E. coli*. (c) Photographs of cultivated *S. aureus* on agar plates and (d) corresponding antibacterial rates of *S. aureus*. (e, f) SEM morphology of *E. coli* and *S. aureus* on various samples. All the data are expressed as means ± SD (n = 3).
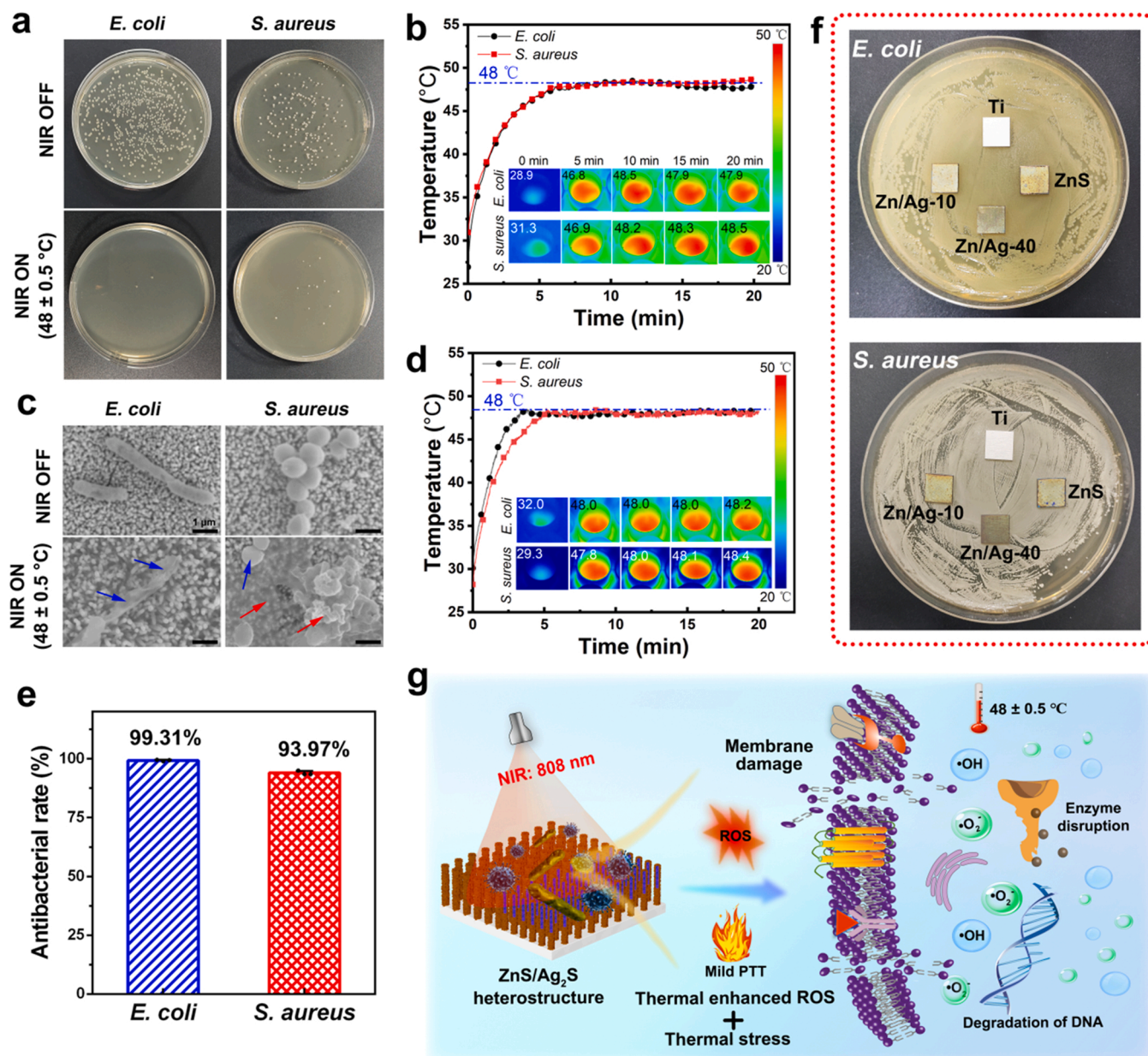
Fig. 8. *In vitro* antibacterial investigation of mild photothermal synergistic photocatalysis upon NIR irradiation without cooling. (a) Photographs of cultivated *E. coli* and *S. aureus* on agar plates, and (b) corresponding photothermal curves. (c) SEM morphology of *E. coli* and *S. aureus* on various samples, and (d) corresponding photothermal curves. (e) Antibacterial rates of *E. coli* and *S. aureus*. (f) Inhibition rings around various samples against *E. coli* and *S. aureus*. (g) The schematic illustration of the antibacterial mechanism of photothermal-enhanced photocatalysis. All the data are expressed as means ± SD (n = 3).

evaluate bacterial-induced inflammation in the peri-implant tissue. A large number of inflammatory cells (green arrows) infiltrated the connective tissue in Ti (NIR-), Ti (NIR+), and Zn/Ag-40 (NIR-) groups. In addition, many bacteria (yellow arrows) were identified in the tissue with Giemsa staining. With 15 min NIR irradiation, the number of inflammatory cells and bacteria in the surrounding tissues of Zn/Ag-40 (NIR+) was drastically reduced due to the effective NIR-responsive antibacterial activity, and no apparent bacterial presence was seen on Giemsa staining. Further H&E staining of the major organs of rats (heart, liver, spleen, lung, and kidney) after treatment showed no discernible (Fig. S15). These results indicate mild photothermal synergistic photothermal-enhanced photocatalysis exhibits excellent *in vivo* antibacterial effects and safety for ZnS/Ag$_2$S heterostructure films.

3.5. Cytocompatibility evaluation

MC3T3-E1 cells were taken to evaluate the cytocompatibility of ZnS/Ag$_2$S heterostructure films (Fig. 10a). Fig. 10b presents the SEM morphology of MC3T3-E1 cells after 1 and 4 days of culture. Compared with Ti, the cells of ZnS, Zn/Ag-10, and Zn/Ag-40 spread well after 1 day and exhibited obvious filopodia and lamellipodia. The surfaces of ZnS, Zn/Ag-10, and Zn/Ag-40 were hydrophilic. The water contact angle was much lower than the Ti surface (Fig. S16), which might be the significant reason for superior cell adhesion and spreading properties of ZnS/Ag$_2$S films [50].

The proliferation results are shown in Fig. 10c. At 1 day, Zn/Ag-10 and Zn/Ag-40 displayed the best cell activity. At 4 days, all samples showed significant proliferation. The trend of cell activity was as follows: Ti > Zn/Ag-40 > Zn/Ag-10 > ZnS. At 7 days, the cell proliferation rates of Ti, ZnS, Zn/Ag-10, and Zn/Ag-40 increased in a mutant manner.
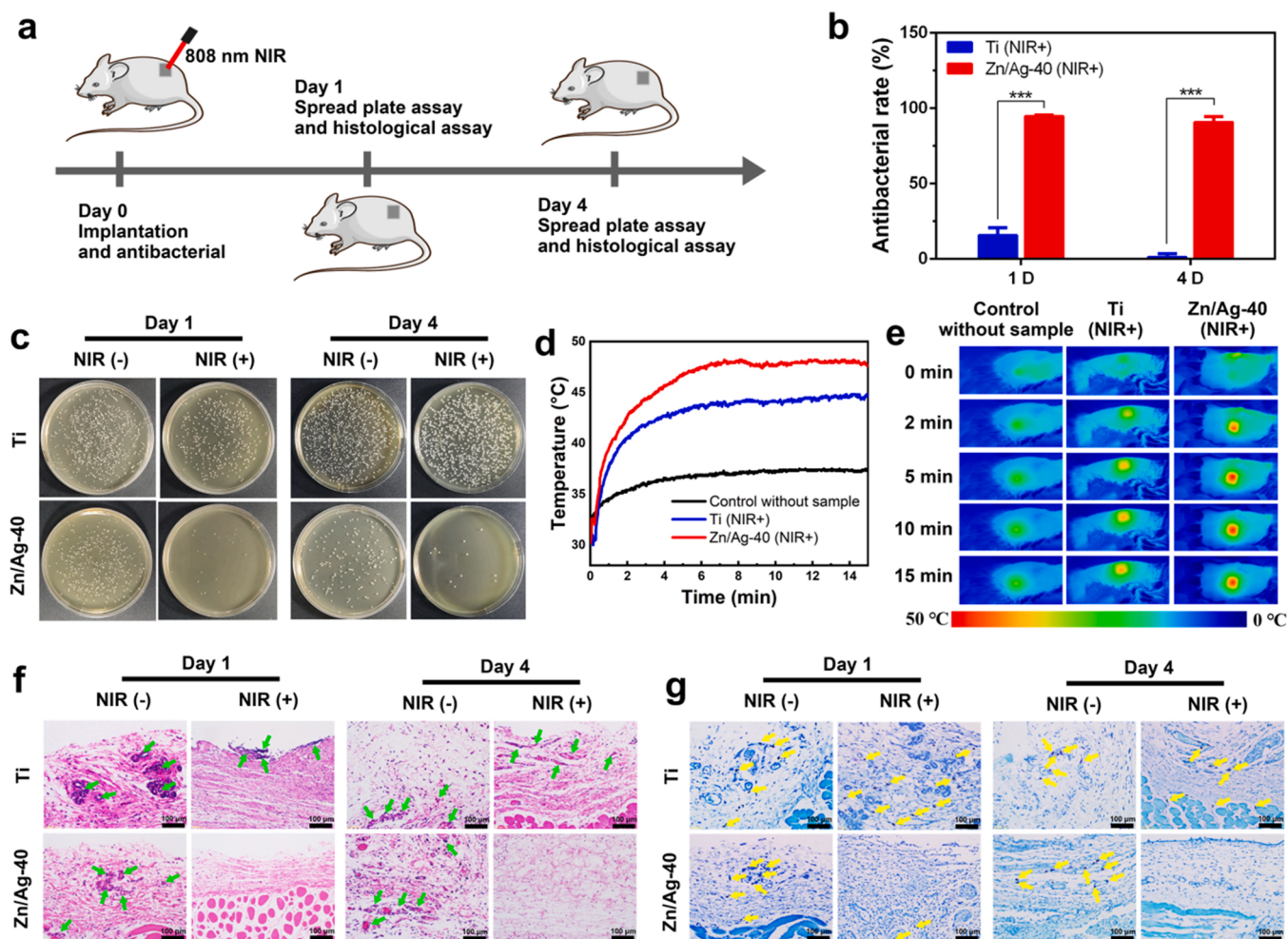
Fig. 9. *In vivo* antibacterial effect of mild photothermal synergistic photocatalysis. (a) The treatment scheme of therapy model through NIR. (b) The bacterial number of spread plate assay in 1 day and 4 days, respectively. (c) Photographs of cultivated *S. aureus* from implanted samples on agar plates. (d) Temperature curves of different samples *in vivo*, and (e) corresponding temperature distribution. (f) Representative images of H&E and (g) Giemsa staining of tissue after 1 day and 4 days. All the data are expressed as means ± SD (n = 3).

Furthermore, the live/dead staining cells suggested that the living cells (green) were dense on ZnS, Zn/Ag-10, and Zn/Ag-40, and almost no dead cells (red) were found (Fig. 10d). The result indicated that ZnS/Ag₂S heterostructure film had good cytocompatibility. In this study, we constructed ZnS/Ag₂S nanorod array films with different Ag₂S shell thicknesses on the biomedical Ti implant. ZnS/Ag₂S straddle-type heterostructure showed excellent NIR photocatalytic ability, rapidly removing bacteria *in vitro* and *in vivo* under the NIR irradiation. The results demonstrate that mild photothermal synergistic photocatalytic antibacterial on the implant was an effective strategy in the clinic.

4. Conclusion

The present study successfully prepared uniform straddle-type ZnS/Ag₂S heterostructure films on titanium, and the thickness of the ZnS core and Ag₂S shell layers was precisely tuned. The ZnS/Ag₂S heterostructure films with appropriate Ag₂S exhibited outstanding NIR photocatalysis. It is exciting that the straddle-type heterostructure promoted the separation of photogenerated electron-hole and generated more ROS under NIR irradiation. The electron transfer mechanism of photocatalytic was proposed. Under NIR excitation, the electrons in the VB of Ag₂S underwent a secondary transition to CB of ZnS, and the electrons in the VB of ZnS jumped to the recombination center of the VB of Ag₂S, leaving holes. Meanwhile, another straddle-type ZnS/Bi₂S₃ heterostructure validated the electron transfer mechanism of the straddle-type

heterostructure. *In vitro* and *in vivo* illustrated that ZnS/Ag₂S heterostructure films possessed good cytocompatibility, and it effectively killed bacteria by mild photothermal synergies photocatalysis. The NIR photocatalysis of straddle-type heterostructure complements the interfacial electron transfer mechanism of the heterostructure. Additionally, it has reference significance for the clinical application of mild photothermal synergistic photocatalytic antibacterial on the implant surface.

CRediT authorship contribution statement

Shiwei Guan: Writing – original draft, Methodology, Investigation, Data curation, Writing – review & editing. **Zhenhao Hou:** Methodology, Experimentation, Writing – review & editing. **Ji Tan:** Conceptualization, Methodology, Investigation, Supervision, Writing – review & editing. **Xianming Zhang:** Materials preparation experimentation, Writing – review & editing. **Junyu Liu:** Animal experimentation. **Huihui Du:** Writing – review & editing. **Hongqin Zhu:** Materials characterization experimentation. **Yuqin Qiao:** Writing – review & editing. **Zixiao Liu:** Methodology. **Xuanyong Liu:** Conceptualization, Writing – review & editing, Supervision, Funding acquisition.

Declaration of Competing Interest

The authors declare that they have no known competing financial interests or personal relationships that could have appeared to influence
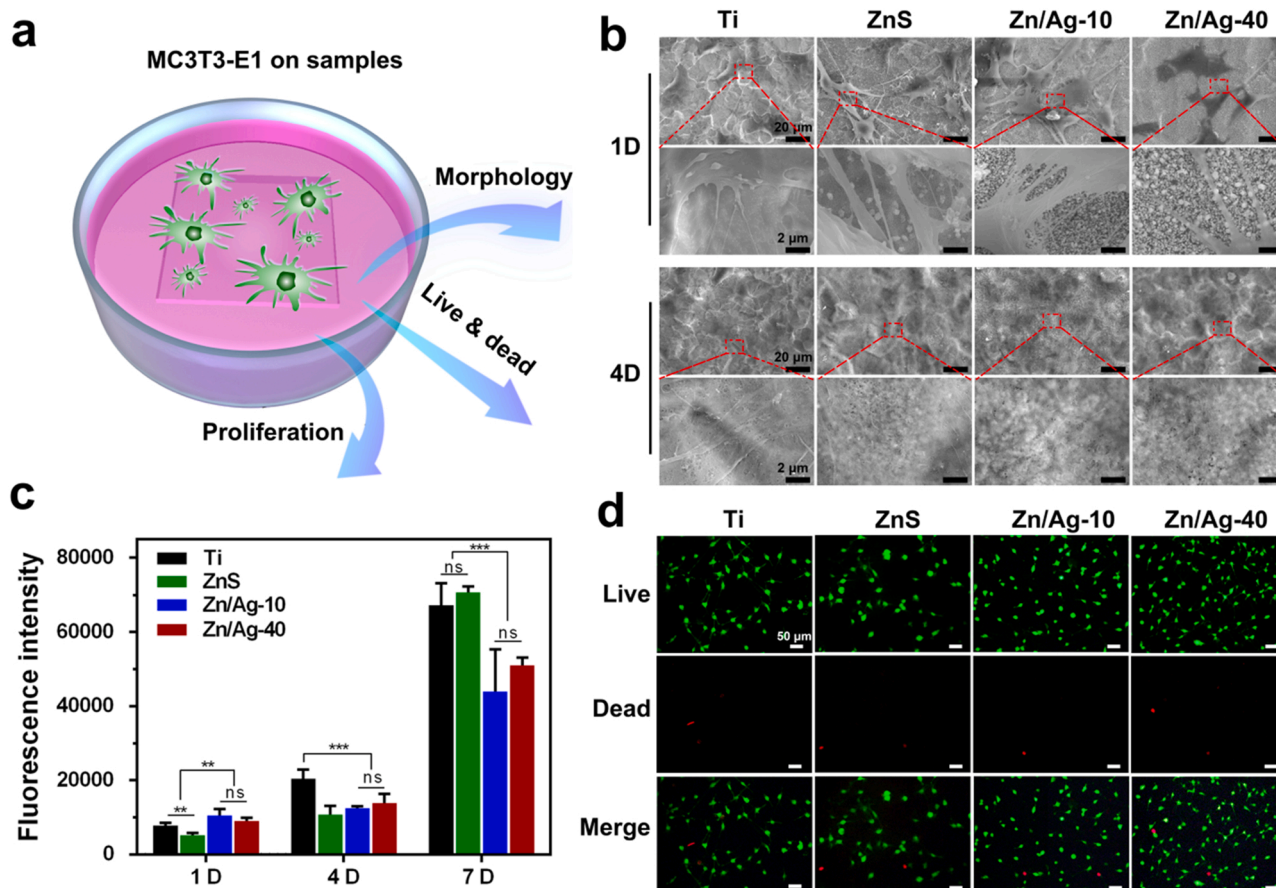
Fig. 10. Biocompatibility of ZnS/Ag$_2$S heterostructure films. (a) Schematic of MC3T3-E1 cells cultured on the samples. (b) SEM morphologies of MC3T3-E1 cultured on sample surfaces for 1 and 4 days. (c) Cell proliferation of MC3T3-E1 cells cultured on various samples. (d) Fluorescent images of live/dead cell staining of MC3T3-E1 cells cultured on various samples for 2 days. All the data are expressed as means $\pm$ SD (n = 3).

the work reported in this paper.

Data Availability

No data was used for the research described in the article.

Acknowledgments

Appendix A. Supporting information

Supplementary data associated with this article can be found in the online version at doi:10.1016/j.apcatb.2023.122826.

References

[1] N.J. Hickok, I.M. Shapiro, Immobilized antibiotics to prevent orthopaedic implant infections, Adv. Drug Deliv. Rev. 64 (2012) 1165–1176.
[2] C.R. Arciola, D. Campoccia, L. Montanaro, Implant infections: adhesion, biofilm formation and immune evasion, Nat. Rev. Microbiol. 16 (2018) 397–409.
[3] L. Wang, X. Fan, M. Gonzalez Moreno, T. Tkhilaishvili, W. Du, X. Zhang, C. Nie, A. Trampuz, R. Haag, Photocatalytic quantum dot-armed bacteriophage for combating drug-resistant bacterial infection, Adv. Sci. 9 (2022), 2105668.
[4] J. Xu, N. Liu, D. Wu, Z. Gao, Y.-Y. Song, P. Schmuki, Upconversion nanoparticle-assisted payload delivery from TiO2 under near-infrared light irradiation for bacterial inactivation, ACS Nano 14 (2019) 337–346.

[5] Q. Chen, H. Zhou, J. Wang, J. Bi, F. Dong, Activating earth-abundant insulator BaSO4 for visible-light induced degradation of tetracycline, Appl. Catal. B: Environ. 307 (2022), 121182.
[6] F. Li, Y. Liu, Q. Chen, X. Gu, W. Dong, D. Zhang, H. Huang, B. Mao, Z. Kang, W. Shi, Transient photovoltage study of the kinetics and synergy of electron/hole co-extraction in MoS2/Ag-In-Zn-S/carbon dot photocatalysts for promoted hydrogen production, Chem. Eng. J. 439 (2022), 135759.
[7] X. Wang, W. Zhou, Y. Wang, L. Gong, X. Liu, X. Zhou, MoO2/Mo heterostructures for hydrogen evolution reaction and ammonia sensing in self-powered mode, Nano Energy 109 (2023), 108253.
[8] S. Kumar, A. Kumar, A. Kumar, V. Krishnan, Nanoscale zinc oxide based heterojunctions as visible light active photocatalysts for hydrogen energy and environmental remediation, Catal. Rev. 62 (2019) 346–405.
[9] E. Kahn, M. Liu, T. Zhang, H. Liu, K. Fujisawa, G. Bepete, P.M. Ajayan, M. Terrones, Functional hetero-interfaces in atomically thin materials, Mater. Today 37 (2020) 74–92.
[10] D. Ramírez-Ortega, A.M. Meléndez, P. Acevedo-Peña, I. González, R. Arroyo, Semiconducting properties of ZnO/TiO$_2$ composites by electrochemical measurements and their relationship with photocatalytic activity, Electrochim. Acta 140 (2014) 541–549.
[11] Y. Gong, J. Lin, X. Wang, G. Shi, S. Lei, Z. Lin, X. Zou, G. Ye, R. Vajtai, B. I. Yakobson, H. Terrones, M. Terrones, B. Tay, Kang, J. Lou, S.T. Pantelides, Z. Liu, W. Zhou, P.M. Ajayan, Vertical and in-plane heterostructures from WS$_2$/MoS$_2$ monolayers, Nat. Mater. 13 (2014) 1135–1142.
[12] L. Wang, T. Huang, G. Yang, C. Lu, F. Dong, Y. Li, W. Guan, The precursor-guided hydrothermal synthesis of CuBi$_2$O$_4$/WO$_3$ heterostructure with enhanced photoactivity under simulated solar light irradiation and mechanism insight, J. Hazard. Mater. 381 (2020), 120956.
[13] Y. Kang, Z. Mao, Y. Wang, C. Pan, M. Ou, H. Zhang, W. Zeng, X. Ji, Design of a two-dimensional interplanar heterojunction for catalytic cancer therapy, Nat. Commun. 13 (2022) 2425.
[14] A.A. Bayode, E.M. Vieira, R. Moodley, S. Akpotu, A.S.S. de Camargo, D. Fatta-Kassinos, E.I. Unuabonah, Tuning ZnO/GO p-n heterostructure with carbon interlayer supported on clay for visible-light catalysis: removal of steroid estrogens from water, Chem. Eng. J. 420 (2021), 127668.
[15] L. Zhang, M. Jaroniec, Toward designing semiconductor-semiconductor heterojunctions for photocatalytic applications, Appl. Surf. Sci. 430 (2018) 2–17.

[16] L. Zheng, F. Teng, X. Ye, H. Zheng, X. Fang, Photo/Electrochemical applications of metal sulfide/TiO2 heterostructures, Adv. Energy Mater. 10 (2019), 1902355.

[17] S. Shen, S.A. Lindley, X. Chen, J.Z. Zhang, Hematite heterostructures for photoelectrochemical water splitting: rational materials design and charge carrier dynamics, Energy Environ. Sci. 9 (2016) 2744–2775.

[18] C. Liu, M. Zhang, H. Geng, P. Zhang, Z. Zheng, Y. Zhou, W. He, NIR enhanced peroxidase-like activity of Au@CeO2 hybrid nanozyme by plasmon-induced hot electrons and photothermal effect for bacteria killing, Appl. Catal. B: Environ. 295 (2021) 120317.

[19] Z. Lian, M. Sakamoto, H. Matsunaga, J.J.M. Vequizo, A. Yamakata, M. Haruta, H. Kurata, W. Ota, T. Sato, T. Teranishi, Near infrared light induced plasmonic hot hole transfer at a nano-heterointerface, Nat. Commun. 9 (2018) 2314.

[20] M. Pang, J. Hu, H.C. Zeng, Synthesis, morphological control, and antibacterial properties of hollow/solid Ag2S/Ag heterodimers, J. Am. Chem. Soc. 132 (2010) 10771–10785.

[21] J. Kim, J. Sun, Y. Zhao, J. Wen, B. Zhou, Z. Zhang, S. Mo, J. Wang, H. Liu, G. Wang, Q. Yu, M. Liu, Electronic structure modulation of Ag2S by vacancy engineering for efficient bacterial infection, Small 18 (2022), 2107807.

[22] H. Yu, W. Liu, X. Wang, F. Wang, Promoting the interfacial H2-evolution reaction of metallic Ag by Ag2S cocatalyst: a case study of TiO2/Ag-Ag2S photocatalyst, Appl. Catal. B: Environ. 225 (2018) 415–423.

[23] H. Li, F. Xie, W. Li, H. Yang, R. Snyders, M. Chen, W. Li, Preparation and photocatalytic activity of Ag2S/ZnS core–shell composites, Catal. Surv. Asia 22 (2018) 156–165.

[24] L. Zhang, P. Li, L. Feng, X. Chen, J. Jiang, S. Zhang, C. Zhang, A. Zhang, G. Chen, H. Wang, Synergetic Ag2S and ZnS quantum dots as the sensitizer and recognition probe: a visible light-driven photoelectrochemical sensor for the "signal-on" analysis of mercury (II), J. Hazard. Mater. 387 (2020), 121715.

[25] Y. Yang, P. He, Y. Wang, H. Bai, S. Wang, J.-F. Xu, X. Zhang, Supramolecular radical anions triggered by bacteria in situ for selective photothermal therapy, Angew. Chem. Int. Ed. 56 (2017) 16239–16242.

[26] Q. Wu, L. Tan, X. Liu, Z. Li, Y. Zhang, Y. Zheng, Y. Liang, Z. Cui, S. Zhu, S. Wu, The enhanced near-infrared photocatalytic and photothermal effects of MXene-based heterojunction for rapid bacteria-killing, Appl. Catal. B: Environ. 297 (2021), 120500.

[27] Y. Fang, X.Y. Yu, X.W.D. Lou, Bullet-like Cu9S5 hollow particles coated with nitrogen-doped carbon for sodium-ion batteries, Angew. Chem. Int. Ed. Engl. 58 (2019) 7744–7748.

[28] K. Xiong, J. Li, L. Tan, Z. Cui, Z. Li, S. Wu, Y. Liang, S. Zhu, X. Liu, Ag2S decorated nanocubes with enhanced near-infrared photothermal and photodynamic properties for rapid sterilization, Colloid Interface Commun. 33 (2019), 100201.

[29] S. Yue, B. Wei, X. Guo, S. Yang, L. Wang, J. He, Novel Ag2S/ZnS/carbon nanofiber ternary nanocomposite for highly efficient photocatalytic hydrogen production, Catal. Commun. 76 (2016) 37–41.

[30] Q. Luo, H. Cao, L. Wang, X. Ma, X. Liu, ZnO@ZnS nanorod-array coated titanium: good to fibroblasts but bad to bacteria, J. Colloid Interface Sci. 579 (2020) 50–60.

[31] R. Han, Y. Xiao, Q. Yang, M. Pan, Y. Hao, X. He, J. Peng, Z. Qian, Ag2S nanoparticle-mediated multiple ablations reinvigorates the immune response for enhanced cancer photo-immunotherapy, Biomaterials 264 (2021), 120451.

[32] Q. Lu, F. Gao, D. Zhao, Creation of a unique self-supported pattern of radially aligned semiconductor Ag2S nanorods, Angew. Chem. Int. Ed. 41 (2002) 1932–1934.

[33] B. Yu, Y. Ji, X. Hu, Y. Liu, J. Yuan, S. Lei, G. Zhong, Z. Weng, H. Zhan, Z. Wen, Heterostructured Cu2S@ZnS/C composite with fast interfacial reaction kinetics for high-performance 3D-printed Sodium-Ion batteries, Chem. Eng. J. 430 (2022), 132993.

[34] J. Xi, H. Xia, X. Ning, Z. Zhang, J. Liu, Z. Mu, S. Zhang, P. Du, X. Lu, Carbon-intercalated 0D/2D hybrid of hematite quantum dots/graphitic carbon nitride nanosheets as superior catalyst for advanced oxidation, Small 15 (2019), 1902744.

[35] B. Barrocas, T.J. Entradas, C.D. Nunes, O.C. Monteiro, Titanate nanofibers sensitized with ZnS and Ag2S nanoparticles as novel photocatalysts for phenol removal, Appl. Catal. B: Environ. 218 (2017) 709–720.

[36] S. Mosleh, K. Dashtian, M. Ghaedi, M. Amiri, A Bi2WO6/Ag2S/ZnS Z-scheme heterojunction photocatalyst with enhanced visible-light photoactivity towards the degradation of multiple dye pollutants, RSC Adv. 9 (2019) 30100–30111.

[37] J. Zhang, B. Zhang, Z. Zheng, Q. Cai, J. Wang, Q. Shu, L. Wang, Tissue-engineered bone functionalized with MoS2 nanosheets for enhanced repair of critical-size bone defect in rats, Adv. Funct. Mater. 32 (2021), 2109882.

[38] Y. Li, Q. Shen, R. Guan, J. Xue, X. Liu, H. Jia, B. Xu, Y. Wu, A C@TiO2 yolk–shell heterostructure for synchronous photothermal–photocatalytic degradation of organic pollutants, J. Mater. Chem. C 8 (2020) 1025–1040.

[39] M. Qiu, D. Wang, H. Huang, T. Yin, W. Bao, B. Zhang, Z. Xie, N. Xie, Z. Wu, C. Ge, Q. Wang, M. Gu, H.L. Kutscher, L. Liu, S. Bao, P.N. Prasad, H. Zhang, A. Regioselectively, Oxidized 2D Bi/BiOx lateral nano-heterostructure for hypoxic photodynamic therapy, Adv. Mater. (2021), e2102562.

[40] L. Wang, X. Zhang, X. Yu, F. Gao, Z. Shen, X. Zhang, S. Ge, J. Liu, Z. Gu, C. Chen, An all-organic semiconductor C3N4 /PDINH heterostructure with advanced antibacterial photocatalytic therapy activity, Adv. Mater. 31 (2019), e1901965.

[41] C. Mao, W. Zhu, Y. Xiang, Y. Zhu, J. Shen, X. Liu, S. Wu, K.M.C. Cheung, K.W. K. Yeung, Enhanced near-infrared photocatalytic eradication of MRSA biofilms and osseointegration using oxide perovskite-based P-N heterojunction, Adv. Sci. 8 (2021), e2002211.

[42] X. Li, B. Kang, F. Dong, F. Deng, L. Han, X. Gao, J. Xu, X. Hou, Z. Feng, Z. Chen, L. Liu, J. Huang, BiOBr with oxygen vacancies capture 0D black phosphorus quantum dots for high efficient photocatalytic ofloxacin degradation, Appl. Surf. Sci. 593 (2022), 153422.

[43] X. Li, Q. Liu, F. Deng, J. Huang, L. Han, C. He, Z. Chen, Y. Luo, Y. Zhu, Double-defect-induced polarization enhanced OV-BiOBr/Cu2−xS high-low junction for boosted photoelectrochemical hydrogen evolution, Appl. Catal. B: Environ. 314 (2022), 121502.

[44] G. Gao, X. Sun, G. Liang, Nanoagent-promoted mild-temperature photothermal therapy for cancer treatment, Adv. Funct. Mater. 31 (2021), 2100738.

[45] X. Dong, J. Ye, Y. Chen, T. Tanziela, H. Jiang, X. Wang, Intelligent peptide-nanorods against drug-resistant bacterial infection and promote wound healing by mild-temperature photothermal therapy, Chem. Eng. J. 432 (2022), 134061.

[46] X. Yu, J. Zhao, D. Fan, A dissolving microneedle patch for antibiotic/enzymolysis/ photothermal triple therapy against bacteria and their biofilms, Chem. Eng. J. 437 (2022), 135475.

[47] I. Burghardt, F. Lüthen, C. Prinz, B. Kreikemeyer, C. Zietz, H.-G. Neumann, J. Rychly, A dual function of copper in designing regenerative implants, Biomaterials 44 (2015) 36–44.

[48] G. Wyszogrodzka, B. Marszalek, B. Gil, P. Dorozynski, Metal-organic frameworks: mechanisms of antibacterial action and potential applications, Drug Discov. Today 21 (2016) 1009–1018.

[49] Y.S. Bae, H. Oh, S.G. Rhee, Y.D. Yoo, Regulation of reactive oxygen species generation in cell signaling, Mol. Cells 32 (2011) 491–509.

[50] S.W. Guan, M. Qi, C. Wang, S.Y. Wang, W.Q. Wang, Enhanced cytocompatibility of Ti6Al4V alloy through selective removal of Al and V from the hierarchical micro-arc oxidation coating, Appl. Surf. Sci. 541 (2021), 148547.